Full Length Article

Graphene oxide-induced CuO reduction in TiO$_2$/CaTiO$_3$/Cu$_2$O/Cu composites for photocatalytic degradation of drugs via peroxymonosulfate activation

Fida Tanos [a,b], Elissa Makhoul [a,c], Amr A. Nada [a,d], Maged F. Bekheet [e], Wiebke Riedel [f], Sarah Kawrani [g], Habib Belaid [a], Eddy Petit [a], Roman Viter [h,i], Victoriia Fedorenko [h], Arunas Ramanavicius [j], Madona Boulos [c], David Cornu [a], Antonio Razzouk [b], Geoffroy Lesage [a], Marc Cretin [a], Mikhael Bechelany [a,k,*]

[a] Institut Européen des Membranes, IEM, UMR 5635, Univ Montpellier, ENSCM, Centre national de la recherche scientifique (CNRS), Place Eugène Bataillon, 34095 Montpellier, France
[b] Laboratoire d'Analyses Chimiques, Faculty of Sciences, LAC—Lebanese University, Jdeidet 90656, Lebanon
[c] Laboratoire de Chimie Physique des Matériaux (LCPM/PR2N), EDST, Université Libanaise, Faculté des Sciences II, Département de Chimie, Fanar, Lebanon
[d] Department of Analysis and Evaluation, Egyptian Petroleum Research Institute, Cairo, 11727, Egypt
[e] Technische Universität Berlin, Faculty III Process Sciences, Institute of Materials Science and Technology, Chair of Advanced Ceramic Materials, Straße des 17. Juni 135, 10623 Berlin, Germany
[f] Freie Universität Berlin, Institut für Chemie und Biochemie, Berlin, Germany
[g] Department of Natural Sciences, Lebanese American University, Chouran, Beirut, 1102-2801, Lebanon
[h] Institut of Atomic Physics and Spectroscopy, University of Latvia, Rainis Blvd., LV-1586 Riga, Latvia
[i] Center for Collective Use of Scientific Equipment, Sumy State University, Sanatornaya Str. 31, 40018 Sumy, Ukraine
[j] Department of Physical Chemistry, Faculty of Chemistry and Geosciences, Institute of Chemistry, Vilnius University, Vilnius, Lithuania
[k] Gulf University for Science and Technology, GUST, Kuwait

ARTICLE INFO

ABSTRACT

Contamination of water bodies is a global environmental and human health issue. Conventional water treatment systems cannot efficiently eliminate organic contaminants, particularly drugs. Photocatalysis is a promising, environmentally friendly oxidation process for the removal of such compounds. A key point is the choice of material to be used as photocatalyst. Here, TiO$_2$/CaTiO$_3$/Cu$_2$O/Cu composites were fabricated by adding different amounts (x) of graphene oxide (GO) (x wt% = 1, 3, and 5 %) to CaCu$_3$Ti$_4$O$_{12}$ powder using the solid-state synthesis method. The produced pellets were sintered under inert nitrogen atmosphere at 1100 °C for 3 h. X-ray diffraction analysis showed that the Cu metal amount was increased upon GO addition, and the UV–Vis diffuse reflectance spectroscopy showed that the spectral response was extended to the visible range. Then, high performance liquid chromatography assessment of paracetamol degradation by a photocatalytic cell using TiO$_2$/CaTiO$_3$/Cu$_2$O/Cu composites with different GO amounts showed that the removal efficiency was increased upon introduction of 0.5 mM peroxymonosulfate (PMS) as active component to generate •SO$_4^-$ radicals. After 3 h under visible light, 96 % of 10 ppm paracetamol was degraded by the composite with 3 % of GO (1 cm^2 surface photocatalyst) compared with 50 % by the composite without GO in the same experimental conditions (PMS in 210 mL of aqueous solution). Free radical trapping and the acute toxicity of potential degradation by-products were also investigated. Our results indicate that TiO$_2$/CaTiO$_3$/Cu$_2$O/Cu with 3 % GO displays long-term stability and durability for the photocatalytic removal of pharmaceutical pollutants from wastewater.

1. Introduction

Fresh water is becoming one of the scarcest resources on Earth, and the availability of safe drinking water is a problem for many countries. Pollution is one of the most important causes of water scarcity and also of environmental disasters and health risks [1–3]. Water sources can be contaminated by many different hazardous contaminants, such as drugs, pesticides, dyes, phenolic compounds, and chemicals used by industries [4,5]. One solution to this issue is to improve wastewater treatment using water recycling techniques that allow adequate filtration and purification [6,7]. However, the removal of organic contaminants by conventional wastewater treatment systems is incomplete (even when present at low concentration) and leads to the generation of more toxic by-products [8,9].

In the last decade, effective and ecofriendly technologies have been developed for the degradation of these difficult-to-remove pollutants [10,11]. For instance, advanced oxidation processes have been tested for the elimination of various pharmaceutical pollutants [12,13]. Photocatalytic degradation is considered a promising method for the degradation of different organic compounds [14]. This technique can convert solar energy into chemical energy that induces radical formation on the semiconductor surface [15,16]. These radicals participate in the redox reactions and improve the fast and non-selective mineralization of trace contaminants [17]. Among the formed radicals, $\bullet SO_4^-$ radicals have a strong oxidation–reduction potential (2.5–3.1 V), long half-life (up to 40 μs), high selectivity, and wide working pH range (from 2 to 8) [18]. The term 'mineralization' is specifically referring to a complex degradation process. This process involves the breakdown of organic matter or compounds. In essence, mineralization represents the transformation of organic substances into their inorganic components, primarily CO_2 and H_2O, through a series of chemical reactions.

Sulfate radical-based AOPs (SR-AOPs) have shown a higher performance in the degradation of biorefractoty pollutants in wastewater treatment. This superiority is related to the various advantages (cited above) [19,20]. The principle of this method is based on the in-situ generation of $\bullet SO_4^-$ radicals trough a precursor salt, peroxymonosulfate (PMS, HSO_5^-). The oxidant PMS can be easily dissolved in water and provide a series of oxidizing processes by breaking O-O bonds due to the long bond distance 1.460 Å [20,21]. Different ways can be used to generate $\bullet SO_4^-$ radicals through the activation of PMS including UV, metal ions, electrochemical, metal oxides, carbon material [19,22,23]. In particular, these radicals are produced by photocatalysis through PMS activation by electrons generated upon exposure to ultraviolet (UV) radiation [24,25]. In recent years, scientists have proposed to combine several activation methods in order to take full advantage of their benefits and reduce their drawbacks [26]. Therefore, in this work we will study the effect of hybrid activation with visible light and transition metal ions and metal oxides.

Titanium dioxide (TiO_2) and calcium titanate ($CaTiO_3$) represent an important class of photocatalysts for organic pollutant removal because of their good photocatalytic activity and stability, chemical inertness, and limited cost [27–30]. However, their wide bandgap energy hinders their utilization under visible light, and the fast electron − hole pair recombination reduces the photocatalytic reaction effectiveness [31–33]. These limitations could be overcome by fabricating heterostructures. Indeed, the formation of heterojunctions is a practical strategy to increase the separation efficiency of photogenerated charge carriers, to reduce the electron-hole pair recombination, and to promote photocatalysis [34,35]. Many research groups have reported the effect of coupling TiO_2 and $CaTiO_3$ for photocatalytic applications [36]. Gao *et al.* showed that a TiO_2-$CaTiO_3$ composite greatly enhances N_2 reduction by photocatalysis [37]. They confirmed that the tight structure between $CaTiO_3$ and TiO_2 improves the separation of the photogenerated charges and increases the number of catalytically active sites [36]. The $CaTiO_3$/TiO_2 heterostructure composites prepared by Lin *et al.* using an *in situ* hydrothermal method strongly increased the

photocatalytic reduction of CO_2 under irradiation and their CO production was 5.6 times higher than that of bare TiO_2 nanosheets [38].

Recently, many researchers have been trying to shift photocatalytic degradation towards the visible light spectrum by coupling TiO_2 with low bandgap semiconductors and by metal doping [39,40]. Copper-based species, such as cuprous oxide (Cu_2O) and metallic copper (Cu^0), are interesting for moving TiO_2 absorption edge towards the visible light region. They also increase the electron-hole pair lifetime and accelerate the charge transport, thus improving TiO_2 photocatalytic features [41–43]. Cu_2O, a p-type semiconductor with a narrow bandgap (~2.2 eV) [43,44], is a good candidate to form a p-n heterostructure with TiO_2 for increasing the optical absorption of visible light [41]. Moreover, Cu-doped TiO_2 is considered a promising catalyst because Cu atoms can be incorporated into the crystal lattice, increasing the absorption of solar irradiation [45,46]. In addition, copper-based materials are excellent catalysts, compared with other transition metals, for PMS activation to produce $\bullet SO_4^-$ radicals [47,48]. The formed Cu^+– $Cu^{[2]+}$ and Cu^{2+}– Cu^{3+} redox pairs can promote $\bullet SO_4^-$ generation *via* PMS activation [49]. Wang *et al.* synthetized Cu^0-Cu_2O using a simple ball-milling method to be used as catalyst for persulfate activation during sulfamerazine degradation under UV light. The Cu^0-Cu_2O/persulfate/UV system completely removed sulfamerazine in 30 min. This shows that Cu^0 and the photoinduced electron transfer from Cu_2O promote Cu^{2+} conversion into Cu^+. In turn, Cu_2O acts as an active site for PMS activation and formation of sulfate radicals [50].

In the last decades, graphene/metal oxide photocatalysts have been investigated to enhance photocatalysis efficiency [51]. Graphene is a two-dimensional material that can be combined with different metal oxides due to its high conductivity, mechanical strength and flexibility, and big specific surface area [51,52]. Graphene derivatives, such as graphene oxide (GO), promote rapid electron transfer by decreasing the charge carrier recombination in metal oxides. For example, Li *et al.* introduced GO into Ag-Cu_2O to form a Ag-Cu_2O/GO ternary nanocomposite for photocatalytic degradation of methyl orange. The nanocomposite displayed excellent photocatalytic activity (90 % of dye eliminated in 60 min) that was much higher than that of Cu_2O and Ag-Cu_2O. Indeed, GO good electrical conductivity facilitates charge transfer and reduces the electron-hole pair recombination [53]. GO can also prevent the degradation of metal oxide nanoparticles in water to prolong the photocatalyst life [52]. Fan *et al.* prepared a series of ZnO-graphene composites by hydrothermal reaction for methyl blue degradation. They observed that such composites significantly inhibited ZnO photodegradation [54]. In addition, transition metals may be partially reduced in oxide materials through GO oxidation during the sintering step [55].

All these works highlight the interest and also the complexity of designing high-performance photo-catalytic systems based on metal oxide-graphene-metal nanocomposites for organic compound degradation. Therefore, it is crucial to find a simple and rapid method to produce photocatalytic heterostructures.

To the best of our knowledge, no study has examined the enhancement of CCTO reduction in the presence of graphene oxide under nitrogen. Furthermore, the heterojunction of CuO, TiO_2, Cu metal, and $CaTiO_3$ for water treatment has not been previously investigated through the activation of peroxymonosulfate.

In this work, we describe the fabrication of new $CaTiO_3$-TiO_2-Cu_2O-Cu heterojunction composites from a $CaCu_3Ti_4O_{12}$ (CCTO) precursor using a one-step sintering process. First, we prepared the pure CCTO powder by ball-milling and thermal treatment. Then, we added different GO amounts to the CCTO powder and pressed them into pellets. After sintering at high temperature in an inert atmosphere, the CCTO composites were decomposed into a mixture of TiO_2, $CaTiO_3$, Cu_2O and Cu. During sintering, GO oxidation changed the Cu_2O-Cu weight fraction and the growth direction of metallic Cu. We then characterized the morphology, structure, and optical properties of the prepared composites, and tested their photocatalytic activity for paracetamol degradation

in the presence of PMS under visible light.

## 2. Experimental section

2.1. Chemicals

Titanium (IV) oxide (TiO_2, CAS Number: 13463–67-7, 99.5 %, Sigma Aldrich), calcium carbonate ($CaCO_3$, CAS Number: 471–34-1, 99.95–100.05 %, Sigma Aldrich), and copper (II) oxide (CuO, CAS Number: 1317–38-0, 98 %, Alfa Aesar) were used to prepare the CCTO powder. Graphite (CAS Number: 7782–42-5, graphite powder < 20 μm, synthetic), sulfuric acid (H_2SO_4, CAS Number: 7664-93-9, 99.999 %), phosphoric acid (H_3PO_4, CAS Number: 7664-38-2, 99.99 %), potassium permanganate ($KMnO_4$, CAS Number: 7722-64-7, 99.0 %), hydrochloric acid (HCl, CAS Number: 7647-01-0, 37 %), and absolute ethanol (CAS Number: 64–17-5), from Sigma Aldrich, were used to prepare GO. Poly (vinyl alcohol) (CAS Number: 9002–89-5, 99 %, Sigma Aldrich) was used as organic binder for pellet preparation. Potassium hydroxide (KOH, CAS Number: 1310–58-3, ≥85 %), OXONE® ($KHSO_5 \cdot 0.5KH$-$SO_4 \cdot 0.5K_2SO_4$, CAS Number: 70693-62-8), and paracetamol ($CH_3CONHC_6H_4OH$, CAS Number: 103–90-2, BioXtra, ≥99.0 %) were from Sigma Aldrich. All reagents were used without any further purification.

2.2. Graphene oxide preparation

Natural graphite powder was used as raw material for GO preparation following the modified Hummer's method [56]. First, 3 g of graphite powder was dissolved in H_2SO_4/H_3PO_4 (9:1) solution by stirring for ~ 5 min. Second, 18 g of $KMnO_4$ was added to the mixture and stirred for 12 h. Upon addition of 3 mL H_2O_2 under vigorous stirring, a brown precipitate was observed. After centrifugation at 600 rpm for 10 min, the precipitate was washed with 30 % HCl solution and then with deionized water and ethanol for several times. The resulting product was dried at 50 °C for 24 h to obtain pure exfoliated GO.

2.3. Synthesis of the pure CaCu3Ti4O12 powder

CCTO powder was prepared using the solid state method. Stoichiometric amounts of CuO, TiO_2 and $CaCO_3$ (as shown in Eq. (1) were mixed by ball milling in an alumina (Al_2O_3) jar with balls (precursors/ball ratio = 1/9; rotation speed = 350 rpm) for 5 h to obtain a homogeneous mixture with nanocrystalline particles. Then, calcination in a muffle furnace under ambient atmosphere at 900 °C for 3 h (heating rate of 5 °C/min) led to the formation of the pure CCTO phase.

$$CaCO_3 + 4TiO_2 + 3CuO \rightarrow CaCu_3Ti_4O_{12} + CO_2 (1)$$
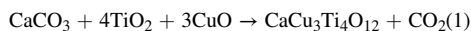
2.4. Preparation of pellets with different graphene oxide amounts

The pure CCTO powder was granulated without and with different amounts (x) of GO (x wt% = 1, 3, and 5 %) by adding poly (vinyl alcohol) as organic binder in an agate mortar. The different powder mixtures were then pressed into pellets (diameter of 10 mm and thickness of 1–2 mm) under a pressure of 5 T, followed by sintering in a tubular furnace at 1100 °C for 3 h (inert nitrogen atmosphere, flow rate of 200 mL min^{-1}, heating and cooling ramp rates set at 2 °C min^{-1}). The treatment under nitrogen atmosphere leads to the decomposition of CCTO as shown in Eq. (2).

$$CaCu_3Ti_4O_{12} \rightarrow CaTiO_3 + 3TiO_2 + 1.5Cu_2O (2)$$
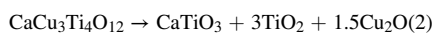
With the presence of CCTO and GO, the reaction in Equation (2) occurs in addition to Equation (3), as follows:

$$CuO \rightarrow Cu + O_2 (3)$$
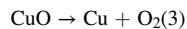
Then, pellets were cooled to room temperature (Fig. 1). Four different pellet types were prepared: pure $TiO_2/CaTiO_3/Cu_2O/Cu$ (CTO-Cu), $TiO_2/CaTiO_3/Cu_2O/Cu/1\%GO$ (CTO-Cu-1GO), $TiO_2/CaTiO_3/Cu_2O/Cu/3GO$ (CTO-Cu-3GO), and $TiO_2/CaTiO_3/Cu_2O/Cu/5GO$ (CTO-Cu-5GO). CTO was used to define the TiO_2 and $CaTiO_3$ phases, whereas Cu indicated the Cu_2O and Cu metal phases. The pellet surface was dry-polished with emery paper (grit number #600) before use. In fact, utilizing pressed pellets as catalyst carriers offers enhanced stability, simplified handling, and efficient recycling, making them the preferred choice for various industrial applications as mention in SI on page 1.

2.5. Physical and chemical characterization of the prepared pellets

The surface morphology was investigated using a Hitachi S4800 scanning electron microscope (SEM). Elemental mapping was obtained with a Zeiss EVO HD15 microscope coupled to an Oxford X-MaxN EDX detector. X-ray diffraction (XRD) measurements were done with a PANAlytical Xpert-PRO diffractometer equipped with an Xcelerator detector using Ni-filtered Cu-radiation with a wavelength of 1.54 Å (scan step size = 0.0020889°/step, time per step = 200.660 sec/step, and 2θ = 20°–80°). The pellets' crystal structure was determined using Rietveld refinement with the FULLPROF software [57] and the profile function 7 (Thompson-Cox-Hastings pseudo-Voigt convoluted with an axial divergence asymmetry function) [58]. The instrument resolution function was obtained from the structure refinement of a silicon standard. Pellets were also characterized by dispersive Raman spectroscopy (HORIBA LABRAM, λ = 659 nm). The laser power was set to 20 W with the following acquisition conditions: continuous mode of 10 s, snapshot time of 7 s, 2.5 number of accumulations set to 30 times. The pellet elemental composition was determined by X-ray photoelectron spectroscopy (XPS) and a monochromatic X-ray source (Al-K_{α}, 1486.6 eV – Resolution FWHM 0.45 eV). Continuous wave (cw) Electron Paramagnetic Resonance (EPR) measurements at 9.78 GHz (X-band frequency), at room temperature, were done with a Bruker B-ER420 spectrometer, upgraded with a Bruker ECS 041XG microwave bridge and a lock-in amplifier (Bruker ER023M), using a Bruker TE$_{102}$ resonator to apply a modulation frequency of 100 kHz. Most measurements were done with a modulation amplitude of 2 G and with 20 dB mw attenuation. Only for the direct comparison with the CCTO reference, a modulation amplitude of 1 G and a 30 dB mw attenuation were chosen. Powdered samples (0.08–0.09 g) were measured in quartz tubes that had an outer diameter of 2.9 mm and a filling height of ~ 10 mm.

2.6. Optical and electrical properties

The pellets' optical bandgap energy was determined with a UV–Vis spectrophotometer (Jasco model V- 570) that had a diffuse reflectance attachment (Shimadzu IRS-2200) in the wavelength range of 200–800 nm. The pellets' charge transport resistance was quantified by electrochemical impedance spectroscopy (EIS) using a Solartron SI 1287 galvanostatic-potentiostat, and 1 M KOH as supporting electrolyte with a three-electrode configuration. CTO-Cu pellets with different GO amounts were used as working electrodes, platinum wire as counter electrode, and Ag/AgCl as reference electrode. The EIS spectra were obtained at 10 mV amplitude, and a frequency range from 0.01 Hz to 10 [5] MHz.

2.7. Paracetamol mineralization

Paracetamol was used as a reference pharmaceutical pollutant to evaluate the CTO-Cu-GO pellet performance for the degradation of organic compounds. All experiments were carried out in a custom-built Teflon cell that contained 210 mL of aqueous solution with 10 ppm paracetamol and 0.5 mmol/L PMS as active components. During the
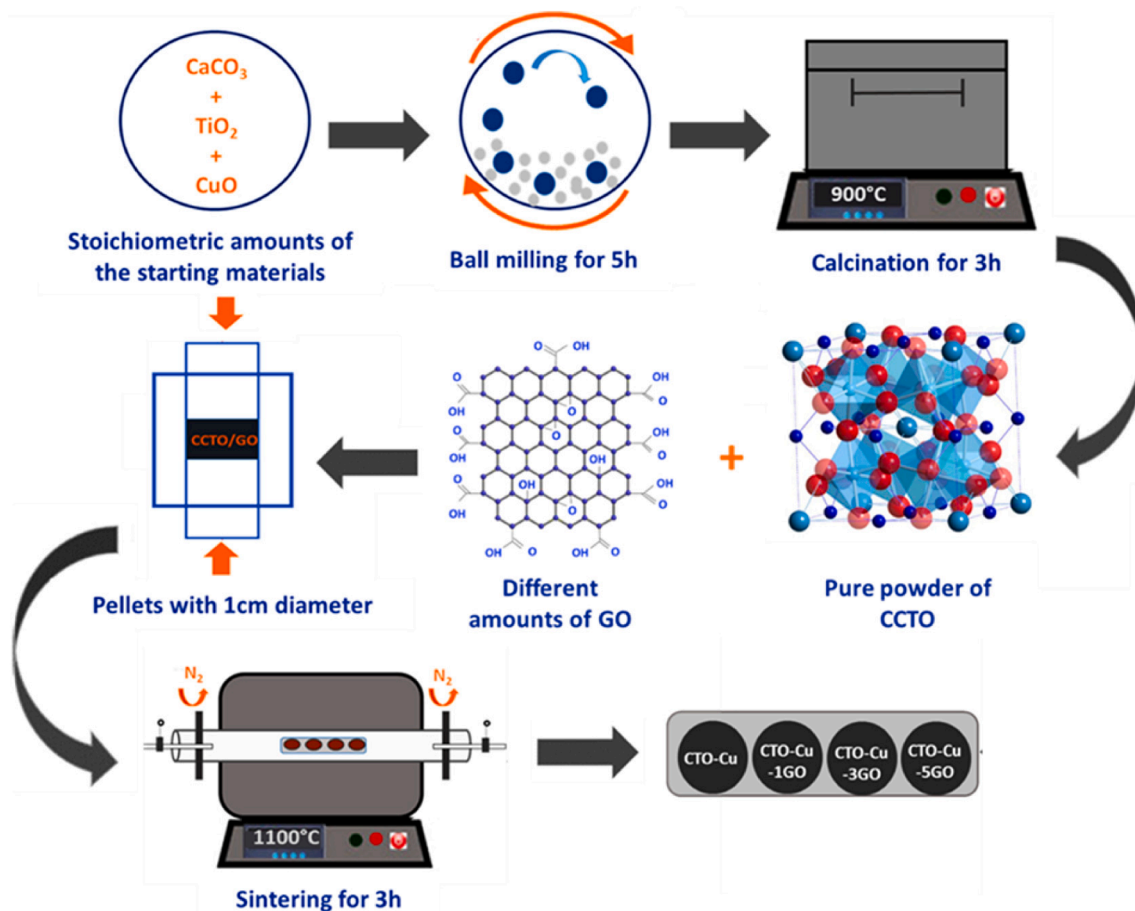
Fig. 1. Schematic illustration of the multi-step CTO-Cu-GO composite synthesis.

experiments, the solution was continuously stirred at 800 rpm. A visible light source (150 W linear halogen lamp; range of 420–600 nm) was used for irradiation. Pellets were positioned vertically in the cell facing the incident light, and the distance between the lamp and the quartz window was maintained at 10 cm. For all experiments, 1 mL aliquots of the solution were collected using a disposable syringe every 30 min (240 min in total) and filtered.

2.8. Analytical methods

2.8.1. High-performance liquid chromatography-mass spectrometry
High-performance liquid chromatography (HPLC) coupled to mass spectrometry (MS) was used to monitor paracetamol concentration in the solution aliquots collected at different time points. The HPLC-MS system included a Waters 2695 pump, autosampler with 20 μL loop, Waters 2695 separation module (HPLC), and Waters Micromass (Wythenshawe, Manchester, UK) Quattro Micro mass spectrometer equipped with electrospray ionization. Separation was carried out using a C18 on a Waters column - XSelect HSS T3 (L = 100 mm, D. I = 2.1 mm and 2.5 μm particles size) column at 25 °C. The mobile phase was 97 % of buffer A (0.1 % formic acid in HPLC-grade water) and 3 % of buffer B (HPLC-grade acetonitrile and 0.1 % formic acid). The flow rate was constant at 0.25 mL min^{-1}, and the run was 3 min. The triple quadrupole MS, coupled to the HPLC instrument, was operated in the positive electrospray ionization mode. MS was adjusted to facilitate ionization in order to achieve the best sensitivity. The detection conditions were: capillary potential 3.5 kV, cone potential 25 V, collision energy 20 V, source temperature 120 °C, desolvation temperature 450 °C, cone gas flow 50 L h^{-1}, and desolvation gas flow 450 L h^{-1}. The nebulizer gas was nitrogen (99.5 % purity).

Paracetamol removal efficiency was calculated with Eq. (1) [59]:

$$Removal\ efficiency(\%) = \frac{(C_0 - C)}{C_0} \cdot 100 \qquad (1)$$

where C_0 (mg L^{-1}) and C (mg L^{-1}) are the paracetamol concentrations in the solution at the initial time t = 0 (min) and at different time points after mineralization initiation under visible light, respectively.

2.9. Scavenger studies

Radical trapping tests with scavengers were carried out to identify the main reactive species implicated in paracetamol degradation. Different scavenger types were added to our system: 0.66 mM of eth-ylenediaminetetraacetic acid (EDTA) and 6.6 mM of p-benzoquinone (p-BQ) to quench holes (h$^+$) and superoxide radicals ($\cdot$O$_2^-$), respectively; 660 mM M *tert*-butyl alcohol (TBA) and 660 mM methanol (MeOH) to quench hydroxyl radicals ($\cdot$OH), and sulfate ($\cdot$SO$_4^-$) and $\cdot$OH radicals, respectively.

2.10. Micro-toxicity tests

To monitor the acute toxicity of by-products generated during paracetamol degradation, the bioluminescence inhibition assay is used to measure the luminescence changes in marine bacteria [60] (the *Vibrio fischeri* LCK 487 strain in this study). Measurements were performed with a Microtox® Model 500 Analyzer (Modern Water Inc.; United Kingdom) coupled to the MicrotoxOmni® software for data analysis. First, 5 mL of reagent diluent was added to allow *V. fischeri* reconstitution at 5 °C. Then, the reagent was stabilized by transferring 200 μL of the solution to the cuvettes at 15 °C for 15 min. *V. fischeri* bacteria were

activated by adding 22 % NaCl solution to the mixture for the dilution to 0.27 % of the initial sample concentration. This dilution was chosen to increase the bioluminescence measurement sensitivity and the detection of acute toxicity, even at extremely low concentrations of toxic compounds. In fact, the presence of toxic elements can reduce *V. fischeri* activity and thus their luminescence. *V. fischeri* luminescence inhibition rate was calculated with Equation (2) [61]:

$$I(t)(\%) = \left(1 - \frac{LU(t)}{R(t)xLU(0)}\right).100 \qquad (2)$$

where LU(t) is the intensity of the luminescence emitted by *V. fischeri* after 5 min or 15 min of contact with the sample, LU(0) is the initial bacterial luminescence intensity before sample addition, and R(t) is the correction term. Indeed, in the absence of toxicity, luminescence decreased over time and due to the action of the environmental conditions. Therefore, the errors due to these factors must be compensated by taking into account the luminescence variability R(t) in a control solution (MilliQ water and NaCl) that gives the LU0(0) value. The correction term R(t) was calculated using Equation (3) [62]:

$$R(t) = \frac{LU0(t)}{LU0(0)}.100 \qquad (3)$$

where LU0(t) is the intensity of the luminescence emitted by *V. fischeri* after 5 min or 15 min of contact with the control solution (MilliQ water and NaCl), and LU0(0) is the initial luminescence intensity before addition of the control solution.

3. Results and discussion

3.1. Characterization of the synthetized composites

CCTO powder was used as precursor to obtain the CTO-Cu-GO composites (Fig. 1). First, the pure CCTO phase was prepared by solid-state synthesis followed by calcination at 900 °C under air for 3 h. Then, pellets were formed by mixing the powder with different GO amounts (1, 3 and 5 %). Finally, pellets underwent sintering at 1100 °C under nitrogen atmosphere to obtain the CTO-Cu-GO samples.

SEM photographs of the prepared CTO-Cu-GO pellets (Fig. 2) indicated that GO addition did not significantly change the sample morphology compared with the CTO-Cu sample. To better understand the sample composition and the element distribution, SEM/EDX

mapping of the sample surface was performed (Fig. S1). This showed the homogeneous distribution of Cu atoms over the CTO-Cu-GO sample surface and confirmed the presence of Ca, Cu, Ti and O elements in all CTO-Cu-GO composites.

The XRD patterns of CTO-Cu, CTO-Cu-1GO, CTO-Cu-3GO, and CTO-Cu-5GO (Fig. 3a) revealed that all samples were composed of four crystalline phases (TiO_2 rutile, $CaTiO_3$, Cu_2O, and metallic Cu), but with different weight fractions. However, neither XRD reflections attributed to GO nor any other crystalline carbon/carbide phase were observed. This might be explained by the destructive oxidation of GO and of any other carbon residues upon sintering. The low content (1, 3 and 5 %) and low scattering ability of GO to X-ray radiations might be another reason. However, the Raman and XPS spectra confirmed GO oxidation in the samples, as discussed below. Therefore, the fabricated samples are TiO_2-$CaTiO_3$-Cu_2O-Cu composites.

The Rietveld refinement method was used to determine the quantity of each crystalline phase in the final samples. The plots of the final Rietveld refinement cycle using the XRD data for CTO-Cu, CTO-Cu-1GO, CTO-Cu-3GO, and CTO-Cu-5GO (Fig. 3b–e) confirmed that TiO_2, $CaTiO_3$, Cu_2O and Cu were the main crystalline phases in all samples after sintering. The quantities of the formed crystalline phases are listed in Table 1. In all samples, TiO_2 rutile was the main phase (45–58 %). The weight fraction of metallic Cu increased and that of the Cu_2O phase decreased upon increasing the amount of GO. These results suggest that Cu_2O is reduced during GO thermal decomposition under N_2, in agreement with the results of our previous work [55]. It has been reported that several transition elements can be reduced by CO oxidation and might be released during the decomposition of carbon-based materials [63,64]. The CTO-Cu-3GO composite contained the highest amount of metallic Cu (24.7 ± 0.1 wt%). The weight fractions of the formed crystalline phases extracted from the Rietveld refinement (Table 1) show that the pure CTO-Cu sample has a small amount of metallic copper (5.7 ± 0.1) and a high percentage of Cu_2O (19.1 ± 0.1). After the addition of 1 % GO, we can see that the weight fraction of metallic copper increases (7.3 ± 0.1) inducing a decrease in the amount of Cu_2O (14.3 ± 0.1). We can realize that an amount of 1 % of GO could reduce Cu^+ to Cu^0 during the oxidation of GO. However, this percentage was not enough to have a strong reduction of Cu_2O. In comparison, by adding 3 % GO, the amount of Cu_2O decreases further to 7.0 ± 0.1 and that of Cu metal increases with the higher content (24.7 ± 0.1). This result means that 3 % GO is the optimal amount to mix with CCTO to induce a strong reduction of

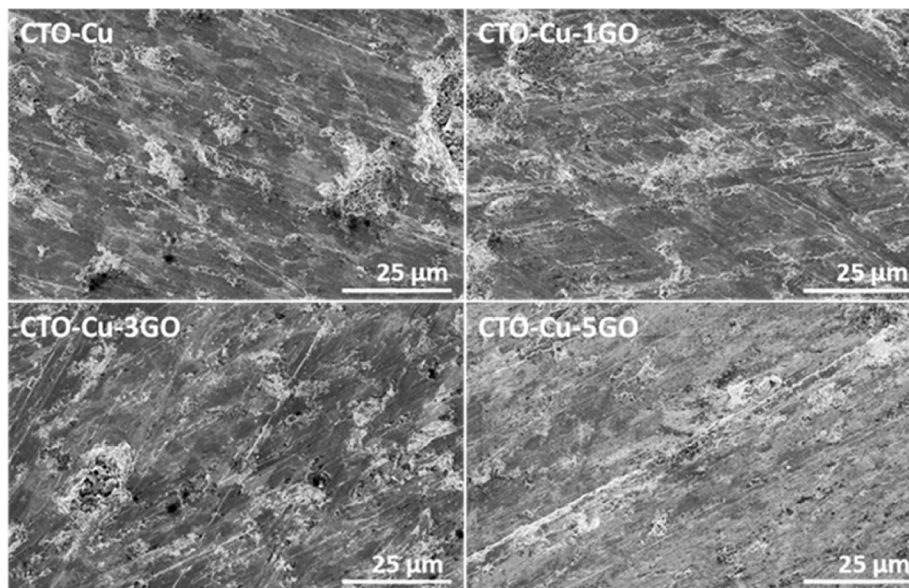**Fig. 2.** Scanning electron micrographs of the CTO-Cu, CTO-Cu-1GO, CTO-Cu-3GO, and CTO-Cu-5GO pellets.
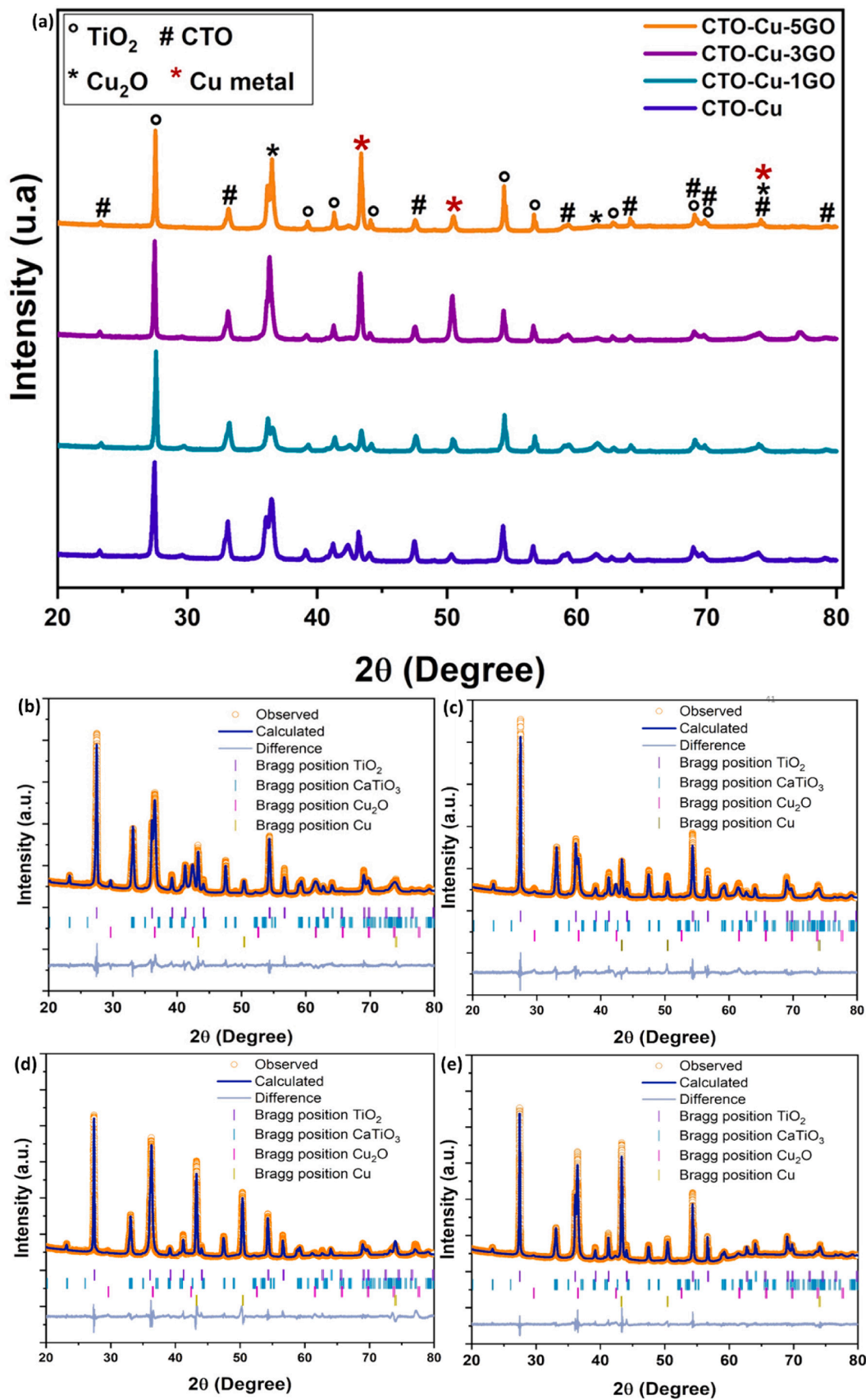
Fig. 3. (a) XRD patterns of the CTO-Cu, CTO-Cu-1GO, CTO-Cu-3GO, and CTO-Cu-5GO composites. (b-e) Structure refinement of the XRD data collected at room temperature for CTO-Cu (b), CTO-Cu-1GO (c), CTO-Cu-3GO (d), and CTO-Cu-5GO (e) pellets after 3-h sintering (1100 °C under nitrogen atmosphere).

Table 1
Weight fractions of the formed crystalline phases extracted from the Rietveld refinement analysis of the *ex situ* XRD patterns for the indicated samples.

Sample	TiO$_2$ rutile (wt. %)	CaTiO$_3$ (wt. %)	Cu$_2$O(wt. %)	Cu metal (wt. %)
CTO-Cu	50.1 ± 0.5	24.1 ± 0.2	19.1 ± 0.1	5.7 ± 0.1
CTO-Cu-1GO	53.0 ± 0.5	25.3 ± 0.2	14.3 ± 0.1	7.3 ± 0.1
CTO-Cu-3GO	44.6 ± 0.5	23.7 ± 0.2	7.0 ± 0.1	24.7 ± 0.1
CTO-Cu-5GO	56.7 ± 0.5	19.8 ± 0.2	8.1 ± 0.1	15.4 ± 0.1

Cu$_2$O to Cu metal upon oxidation of this 3 % GO. However, with 5 % GO, only 15.4 ± 0.1 of metallic Cu was obtained. This result suggests that the agglomeration of GO with an amount of 5 % limits the reduction process of Cu$^+$ to Cu^0. Therefore, 3 % GO was the optimal amount to use as precursor in the starting material to have the highest Cu content after sintering at 1100 °C under nitrogen. The utilization of a temperature of 1100 °C was a deliberate choice to secure the stability of the resultant composite. This high temperature served two essential purposes: firstly, it enabled the composite to undergo a thermal treatment that enhanced its stability, and secondly, it facilitated the transformation of CuO into Cu$_2$O and Cu metal during the oxidation of GO. This elevated temperature played a pivotal role in the thermal treatment and crystalline phase alteration of the composite, ultimately yielding a material with heightened stability and resilience.

We should notice that the decomposition of CaCu$_3$Ti$_4$O$_{12}$ occurs at 1100 °C, resulting in the generation of TiO$_2$ and CaTiO$_3$. With the Ca to Ti ratio in CaCu$_3$Ti$_4$O$_{12}$ being 1:4, the anticipated ratio of CaTiO$_3$ to TiO$_2$ should ideally be 1:3. However, this deviates from the approximately 1:2 ratio indicated in Table 1. Notably, this ratio is determined through XRD, a technique that solely identifies the crystalline portion. The presence of other amorphous compounds/phases may be a contributing factor, potentially causing a deviation in this ratio. Therefore, our future objective is to conduct additional experiments to rectify and comprehend the origin of this deviation in the ratio. This approach aims to enhance the accuracy of the CaTiO$_3$ to TiO$_2$ ratio by addressing any potential influences from the presence of amorphous compounds or phases, thus refining the overall understanding of the material composition.

The XRD reflection corresponding to the (1 1 1) plane of the rutile TiO$_2$ phase was highly asymmetric in the CTO-Cu sample (Fig. S2), but became symmetric in the CTO-Cu-5GO composite due the higher GO amount. The use of 5 % GO as starting material with CCTO leads to the oxidation of this amount which induces the reduction of Cu^{2+} to Cu$^+$ and Cu^0. This reduction led to the decrease of the microstrain and to obtain a symmetrical plane (1 1 1) of the TiO$_2$ phase. The asymmetric shape of the XRD reflections could be explained by the high microstrain or the presence in the samples of several TiO$_2$ phases with different oxidation states of Ti ions. The Rietveld refinement analysis highlighted the high microstrain in all crystalline phases that decreased with the increasing GO amount used (Table 2). These results suggest that the asymmetric shape of the XRD reflections (Fig. S2) is due to the high microstrain. The Cu^0 and Cu$_2$O grains were preferentially grown along the [2 0 0] and [1 1 1] directions, respectively, in the CTO-Cu-3GO

Table 2
Microstrain of the formed crystalline phases extracted from the Rietveld refinement analysis of the *ex situ* XRD patterns for the indicated samples.

Microstrain x10^{-3}				
Sample	TiO$_2$ rutile	CaTiO$_3$	Cu$_2$O	Cu metal
CTO-Cu	3.40 ± 0.02	2.60 ± 0.02	5.70 ± 0.02	2.60 ± 0.02
CTO-Cu-1GO	2.80 ± 0.02	2.90 ± 0.02	5.50 ± 0.02	2.50 ± 0.02
CTO-Cu-3GO	2.00 ± 0.02	2.50 ± 0.02	4.60 ± 0.02	2.50 ± 0.02
CTO-Cu-5GO	1.400 ± 0.02	2.60 ± 0.02	4.30 ± 0.02	2.20 ± 0.02

sample, while both phases were preferentially grown along the [1 1 1] direction in the CTO-Cu-5GO sample. Conversely, no preferred orientation was observed for all crystalline phases in the CTO-Cu and CTO-Cu-1GO samples. The preferred orientation of the metallic Cu^0 phase along the [2 0 0] direction in the CTO-Cu-3GO sample could partly explain its high photocatalytic activity (see section 3.2). In fact, a reduction in the microstrain is reflected in a considerable increase in the surface area, which improves photocatalytic activity by increasing significantly the number of adsorption sites to breakdown more para-cetamol molecules [65].

In the next step, Raman spectroscopy was used to determine the main phase of the CTO-Cu materials. All plots exhibited three defined bands (142, 443 and 610 cm^{-1}, respectively) that corresponded to the B$_{1g}$, E$_g$ and A$_{1g}$ modes, characteristic of the TiO$_2$ rutile phase [66,67] (Fig. 4a). Moreover, the band at 237 cm^{-1} corresponded to the second-order scattering feature [68,69]. Besides these distinctive vibrations, no additional peak was observed for the other phases, possibly because they overlapped with the broad bands of pure TiO$_2$ rutile. In addition, no characteristic peak associated with the D and G bands of GO was observed in the Raman spectra of all samples (Fig. S3), confirming GO oxidation during sintering. The mechanism of GO oxidation will be further investigated through thermal analysis at a later stage. The release of CO$_2$ and C, monitored by in-situ mass spectrometry, will be attributed to the oxidation of GO during the thermal decomposition of CCTO. Notably, the MS signals associated with C and CO$_2$ gases in the CTO-Cu-GO samples will surpass those in the CTO-Cu sample, providing clear evidence of the oxidation of GO in the CTO-Cu-GO samples.

XPS gave additional information on the chemical composition and oxidation state of different elements in the CTO-Cu composites. The high-resolution XPS scans of Ti 2p, O 1s, Cu 2p and N 1s for the pure CTO-Cu sample and the CTO-Cu-3GO sample are shown in Fig. 4b–e. The Ti 2p spectrum could be fitted with two peaks at 457.98 and 458.87 eV, corresponding to Ti^{3+} 2p$_{3/2}$ and Ti^{4+} 2p$_{3/2}$ (Fig. 4b), suggesting that Ti^{4+} is reduced to Ti^{3+} during GO oxidation [34,40,46,70]. The O 1s spectra (Fig. 4c) displayed a peak at 529.43 eV, attributed to the Ti/Cu-O bond, and another peak at 532.08 eV, assigned to Ti/Cu-OH bonds. These results indicate strong interactions within the TiO$_2$-CaTiO$_3$-Cu$_2$O heterojunction [40,41,71,72]. The Cu 2p spectra (Fig. 4d) were characterized by two peaks at 933 and 953 eV that corresponded to the Cu 2p$_{3/2}$ and Cu 2p$_{1/2}$ peaks of Cu$^+$ and Cu^0, respectively. Although Cu$^+$ and Cu^0 cannot be differentiated easily because of their small difference in binding energy [73,74], the XRD results clearly demonstrated the existence of Cu$_2$O and metallic Cu^0 in the CTO-Cu composites. The peaks at 934 and 954 eV corresponded to the Cu 2p$_{3/2}$ and Cu 2p$_{1/2}$ peaks of Cu^{2+}, respectively. Cu^{2+} presence was confirmed also by the shake-up satellite at 943 eV [72,75–78]. Cu^{2+} detection at the sample surface was in line with the EPR results. The Cu 2p spectra strongly changed upon addition of 3 % GO. Specifically, in the CTO-Cu-3GO sample, the Cu^{2+} peaks were shifted to lower binding energies, suggesting partial reduction of CuO to Cu$_2$O and Cu^0 during sintering under N$_2$ in the presence of GO [55,75,79]. The decrease in Cu$_2$O amount at the surface after GO addition suggests a GO reduction effect during sintering and is in agreement with the XRD and EPR data. The Cu^0 ratio significantly increased, whereas Cu^{2+} and Cu$^+$ decreased due to GO oxidation at high temperatures, leading to CuO reduction to metallic Cu^0. The absence of CuO reflections in the resulting XRD pattern (see Fig. 3) could be explained by the small CuO amount, low crystallinity degree, or small cluster sizes. Finally, in the N s1 spectra (Fig. 4e), a single peak at 399.97 eV was detected. This typical peak corresponded to interstitial N [80]. A common peak at 284.8 eV, which corresponds to C–C bonds, was observed in the XPS spectra of C 1s for the GO, CTO-Cu and CTO-Cu-3GO samples (Fig. S4). Unlike what observed in the GO spectrum, no peak was detected at higher binding and corresponding to C-O and O–C = O bonds for the CTO-Cu-3GO sample. This confirmed GO oxidation during sintering under N$_2$ atmosphere. These results are in good agreement with the XRD and Raman data. Carbon detection in the pure CTO-Cu
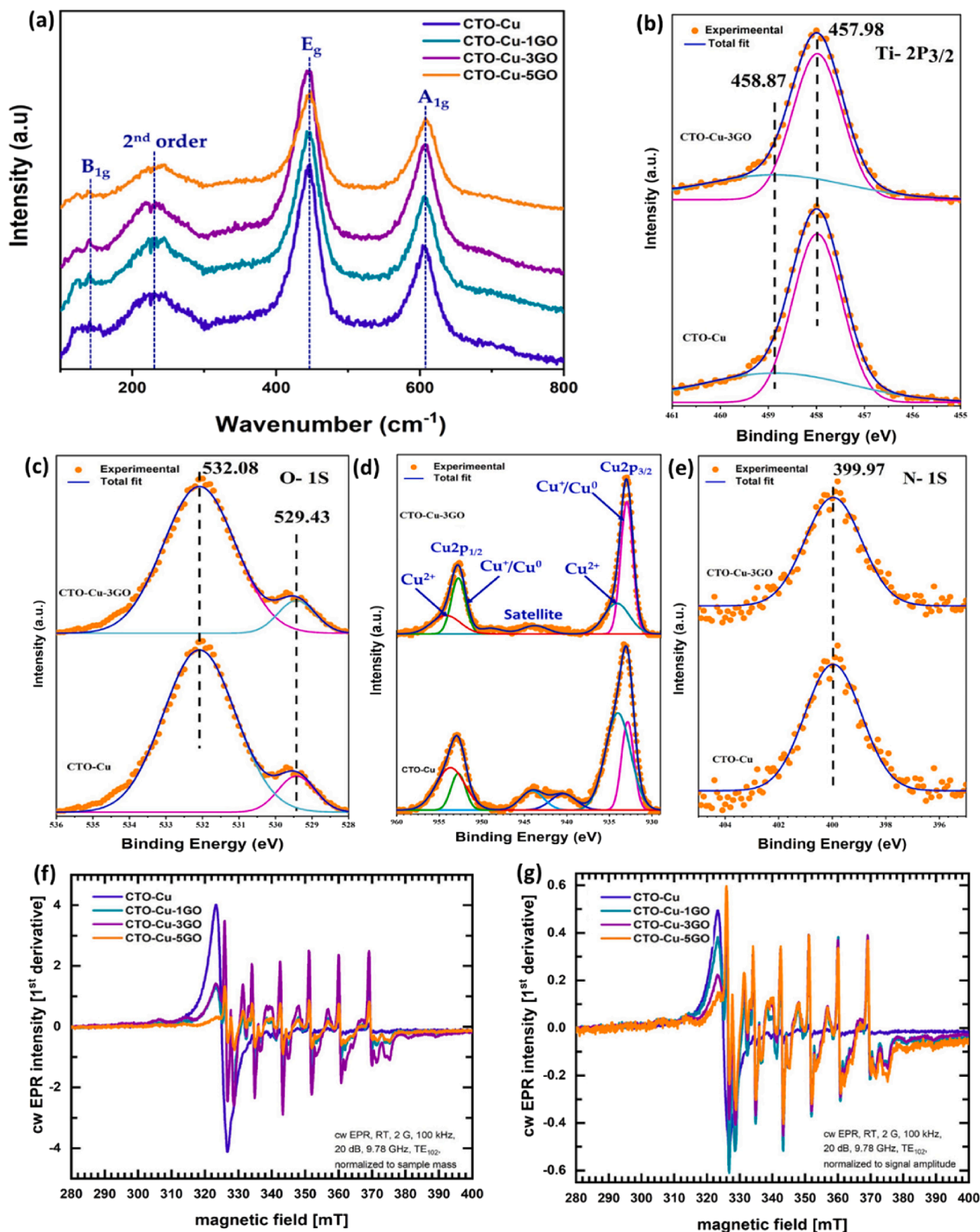
Fig. 4. (a) Raman shifts of the CTO-Cu, CTO-Cu-1GO, CTO-Cu-3GO, and CTO-Cu-5GO pellets. (b-e) High resolution XPS spectra of Ti 2P3/2 (b), O 1S (c), Cu 2P3/2 (d), and N 1 s (e) for the CTO-Cu and CTO-Cu-3GO samples. (f-g) Room-temperature cw EPR spectra of CTO-Cu-1GO, CTO-Cu-3GO, CTO-Cu-5GO, and CTO-Cu normalized to the sample mass (f) and to the signal amplitude (2 G modulation amplitude, 20 dB mw attenuation) (g).

sample can be attributed to the PVA used as organic binder during pellet preparation and/or to the carbon felt support placed inside the alumina boat used for sintering.

The XPS results were confirmed by the EPR measurements. Compared with CCTO, in the cw EPR spectra of the CTO-Cu sample (fig. S5a-b), the signal intensity of the broad Cu^{2+} EPR signal at g = 2.15 was strongly decreased (by a factor of ~ 2800). This is in line with other results indicating Cu^{2+} reduction to Cu^+ or Cu^0 in the CTO-Cu sample. However, the ΔB_{pp} linewidth of the weak Cu^{2+} signal was comparable in the CTO-Cu sample and in the CCTO reference (35 G vs 32 G), suggesting similar interactions for the residual Cu^{2+} species in the two samples. This could indicate the presence of small amounts of residual CCTO in the CTO-Cu reference.

Comparison of the cw EPR spectra (obtained at room temperature) of the CTO-Cu, CTO-Cu-1GO, CTO-Cu-3GO and CTO-Cu-5GO samples (Fig. 4f, g) indicated that the CTO-Cu reference displayed the highest, but still very weak, Cu^{2+} signal (between 310 and 330 mT). The (absolute) intensity of the Cu^{2+} signal was similar in the CTO-Cu-1GO and CTO-Cu-3GO samples and was higher than in the CTO-Cu-5GO sample. Next to the broad Cu^{2+} line, all samples displayed signals that were attributed to Mn^{2+} species (between 335 and 380 mT), presumably due to small amounts of Mn impurities linked to the use of potassium permanganate during GO preparation. The absence of Mn detection by XPS suggests minimal amounts of Mn impurity in the samples (<0.1 at%).

Oxygen vacancies are expected to be produced in the final composites with the partial reduction of Ti^{4+} and Cu^{2+} induced by the oxidation of GO. However, it is quite challenging to accurately determine oxygen vacancies in the obtained composites by fitting XPS spectra. As a result, EPR analysis was conducted on CTO-Cu and CTO-Cu-GO samples. Fig. 4f, g show that all the samples display a broad Cu^{2+} signal indicating Cu^{2+} reduction to Cu^+ or Cu^0. However, it should be noted that these EPR measurements cannot completely exclude changes in the existence or amount of oxygen vacancies, as only paramagnetic oxygen vacancies may be detected by EPR.[55].

As the photocatalytic activity is strongly related to the material optical absorption capacity in the visible light region, the optical bandgap of the CTO-Cu-GO composites and their capacity to adsorb light were assessed by UV–Vis absorption spectroscopy. This analysis showed the presence of two absorption bands: one at ~ 385 nm in the UV region, which corresponded to TiO_2 bandgap energy of 3.2 eV, and one at 400–600 nm, which indicated the presence of Cu^{1+} and $(Cu–O–Cu)^{2+}$ clusters in the partially reduced CuO matrix (Fig. 5a). This confirmed the co-existence of Cu metal and Cu_2O, in line with the XRD data [81]. The energy bandgap values, estimated from the Tauc plot (Fig. 5b) were 2.53 ± 0.02, 2.39 ± 0.02, 2.28 ± 0.01, and 2.61 ± 0.03 eV for CTO-Cu, CTO-Cu-1GO, CTO-Cu-3GO, and CTO-Cu-5GO, respectively. Therefore, all fabricated composites could adsorb visible light due to the combination of TiO_2 with metallic Cu^0 and Cu_2O. After GO addition, a slight redshift was observed in the optical bandgaps with the increase of Cu amount.

The CTO-Cu-3GO sample had the lowest bandgap value, due to the increase in metallic Cu^0 content. These results are in good agreement with previous studies [82,83]. The redshift can be explained by incorporation of Cu ions in the TiO_2 lattice to ensure charge balance after rearrangement of the neighboring atoms, resulting in the lattice deformation. The lattice deformation, caused by Ti^{4+} substitution with Cu^{2+}, affects the electronic structure of the TiO_2 crystalline lattice, thus modifying TiO_2 optical absorption [84,85]. Conversely, absorption in the visible light region by the CTO-Cu-5GO sample was decreased due to the lower Cu metal content.

The photocatalytic activity of the semiconductor is highly connected to its optical absorption capacity in the visible range. According to the literature, the band gap values of photocatalysts diminish progressively as the quantity of metallic copper increases due to the incorporation of copper ions into the TiO_2. The XRD data demonstrate that CTO-Cu-3GO contains the highest amount of metallic copper when compared to the other samples. In addition, the XPS analysis indicates that the oxidation of GO results in the partial reduction of CuO to metallic copper in the CTO-Cu-3GO. Furthermore, the EPR measurement confirm the XPS data by providing additional information on the the signal intensity of the broad Cu^{2+} EPR signal, confirming the reduction of Cu^{2+} to Cu^+ and Cu^0. As a result, the presence of copper ions modifies the electronic structure of the TiO_2 crystalline lattice, resulting in a change in optical absorption to the visible light region, particularly in the case of the CTO-Cu-3GO sample [83,84]. These findings align with the results obtained from XRD and XPS analyses, providing further confirmation of the effective incorporation of copper into the TiO_2 lattice.

The transfer efficiency of the photogenerated electron-hole pairs was investigated by EIS. A smaller arc radius in the Nyquist plot indicates higher charge transfer capacity and faster separation of photoinduced carriers [86–88]. The results were fitted with the Z-View software using the representative equivalent electrical circuit of $R_\Omega + Q_{CPE}//R_{ct}$ where R_Ω is the electrolyte resistance, Q_{CPE} the constant phase element, and R_{ct} the charge transfer resistance. Comparison of the Nyquist plots (Fig. 5c) showed that the pure CTO-Cu sample had the largest semi-circle, indicating the highest resistance. The semi-circle diameter decreased upon GO addition, especially in the CTO-Cu-3GO sample that displayed the smallest arc radius.

For the quantitative analysis, Table 3 shows the R_Ω and R_{ct} values. Comparison of the resistance values (CTO-Cu > CTO-Cu-1GO > CTO-Cu-

Table 3
EIS parameters in the tested catalysts.

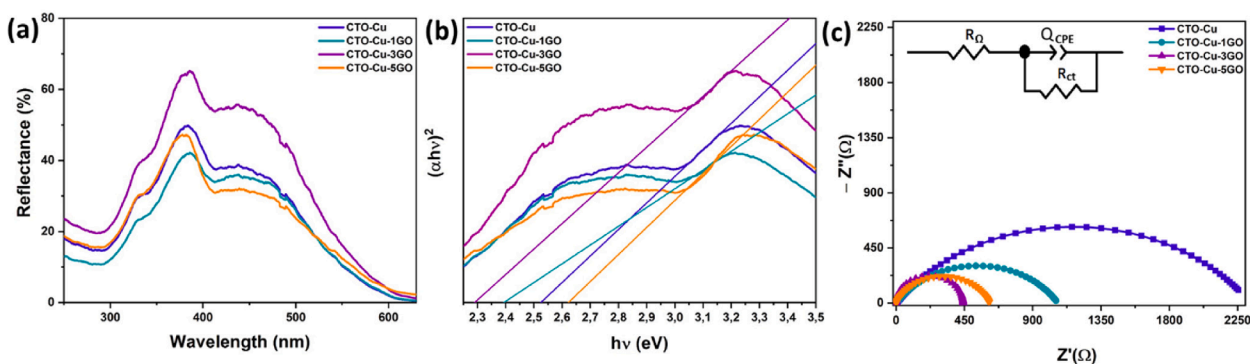| Sample	$R\Omega$ (Ohm)	R_{ct} (Ohm)
CTO-Cu	2.8	2227.8
CTO-Cu-1GO	5.9	1053.1
CTO-Cu-3GO	1.4	438.6
CTO-Cu-5GO	1.3	610.7

Fig. 5. (a) UV–Vis diffuse reflectance spectroscopy. (b) Tauc plot;.(c) Electrochemical impedance spectroscopy data of CTO-Cu, CTO-Cu-1GO, CTO-Cu-3GO and CTO-Cu-5GO samples (sintered at 1100 °C under nitrogen for 3 h) as Nyquist plots.

5GO > CTO-Cu-3GO) indicated that CTO-Cu-3GO displayed the most rapid interfacial charge migration. This could be related to the effective separation of electron-hole pairs induced by the increase of metallic Cu^0 concentration with 3 % of GO and the incorporation of CTO, Cu_2O and Cu in TiO_2. The resistance increase in the CTO-Cu-5GO sample is in agreement with its large bandgap energy value.

Since the CTO-Cu-3GO sample has the lowest resistance among all catalysts, cyclic voltammetry was performed using this pellet under dark and visible conditions to compare the effect of irradiation on the current response. Fig. S6 shows the CV curves of catalyst in 1 M KOH as electrolyte at a scan rate 25 mV. s^{-1}. It can be seen that the current intensity of the anodic and cathodic peaks increases after exposure to visible light irradiation. The CTO-Cu-3GO pellet showed an improved photocurrent response due to the rapid migration, and separation of photo-generated electron-hole pairs to enhance the redox reactions.

3.2. Photocatalytic degradation of paracetamol

The CTO-Cu-GO pellets' photocatalytic activities were investigated by monitoring the degradation of 10 ppm paracetamol in 210 mL of aqueous solution in the presence of PMS. The solution was maintained under stirring throughout the entire degradation period. All the catalysts were utilized in the form of pellet, positioned vertically within the cell to directly face the incident light. After 180 min under visible light, the pure CTO-Cu sample led to the lowest paracetamol removal rate (50 %) compared with CTO-Cu-1GO, CTO-Cu-3GO and CTO-Cu-5GO (60 %, 96 % and 80 %, respectively)(Fig. 6). The finding that the highest paracetamol degradation rate was obtained with the catalyst that contained 24.7 wt% of Cu (i.e. CTO-Cu-3GO) suggests that the degradation efficiency increases with the Cu content. In agreement, paracetamol removal by CTO-Cu-5GO, which includes only 15.36 wt% of Cu, was 16 % lower than with CTO-Cu-3GO. These results indicate that the synergistic effects of the TiO_2-CTO-Cu_2O-Cu heterojunction strongly improve the photocatalytic efficiency under visible light. This can be explained by the following roles of the three phases: (i) the $CaTiO_3$ phase and copper species may increase the charge transfer in the CTO-Cu-3GO composite, as already indicated by the EIS data, to produce a higher number of active radical species and reduce the electron-hole pair recombination during the photocatalytic process [38,45,89]; and (ii) the Cu species contribute to shift the absorption to the visible spectrum (see the UV reflectance results), strongly increasing paracetamol removal under visible light [83,90]. Furthermore, TiO_2 rutile plays a dual role within our catalyst system: Firstly, it functions as a robust structural support material, ensuring the composite's endurance and stability

throughout extended photocatalytic processes. This stability is pivotal for practical applications, as it safeguards the catalyst's structural integrity over prolonged use. Additionally, rutile operates as a co-catalyst, actively engaging in redox reactions and augmenting the separation of charge carriers when partnered with other materials like $CaTiO_3$, Cu_2O, and Cu metal. This collaboration yields synergistic effects that heighten the overall efficiency of the photocatalytic process. By adopting this multi-material strategy, we can effectively mitigate the limitations associated with rutile's individual photocatalytic performance, all while leveraging its structural support and co-catalytic contributions to attain superior overall performance. In addition, the preferred orientation of the metallic Cu^0 phase along the [200] direction relates to the enhanced photocatalytic activity in the CTO-Cu-3GO composite. This particular orientation is instrumental in promoting efficient charge transport within the material by minimizing electronic obstacles. As a result, it enables electrons and holes generated during photocatalysis to traverse the material more freely. This assertion is supported by impedance measurements, where the CTO-Cu-3GO sample exhibited notably accelerated interfacial charge migration compared to the other samples. In the [200] oriented Cu^0 phase, these charge carriers are more likely to be spatially separated, reducing the recombination and increasing the chances of participating in redox reactions.

In order to verify the importance of combining different metal oxides, the performance of our catalysts was compared to $CaTiO_3$ and TiO_2 pellets on the photocatalytic degradation of paracetamol using the same conditions as mentioned in section 2.7. The results (Fig. S7) indicate a degradation of 46 % and 32 % of paracetamol after 4 h using $CaTiO_3$ and TiO_2 pellets, respectively. The comparison of the efficiency of these catalysts with our CTO-Cu-3GO catalyst confirms the necessity of combining TiO_2, $CaTiO_3$, Cu metal, and Cu_2O.

An ideal photocatalyst for the degradation of organic pollutants should be stable and reusable. The CTO-Cu-3GO composite durability was evaluated by measuring paracetamol degradation using the same catalyst for five cycle. After each cycle, the CTO-Cu-3GO sample was washed in deionized water and used again. Paracetamol degradation was not affected after five cycles (Fig. 7a), indicating that the photocatalyst is stable and can be reused to degrade pharmaceutical pollutants under visible light. In order to evaluate the effect of 5 cycles of degradation on the same CTO-Cu-3GO photocatalyst, SEM analysis was performed on the surface of the used pellet compared to the fresh sample. Fig. S8 shows the SEM images of CTO-Cu-3GO photocatalyst before and after 5 cycles of degradation, no significant change is detected after degradation which indicates the maintenance of the morphology of the heterostructure composite CTO-Cu-3GO after its reuse.
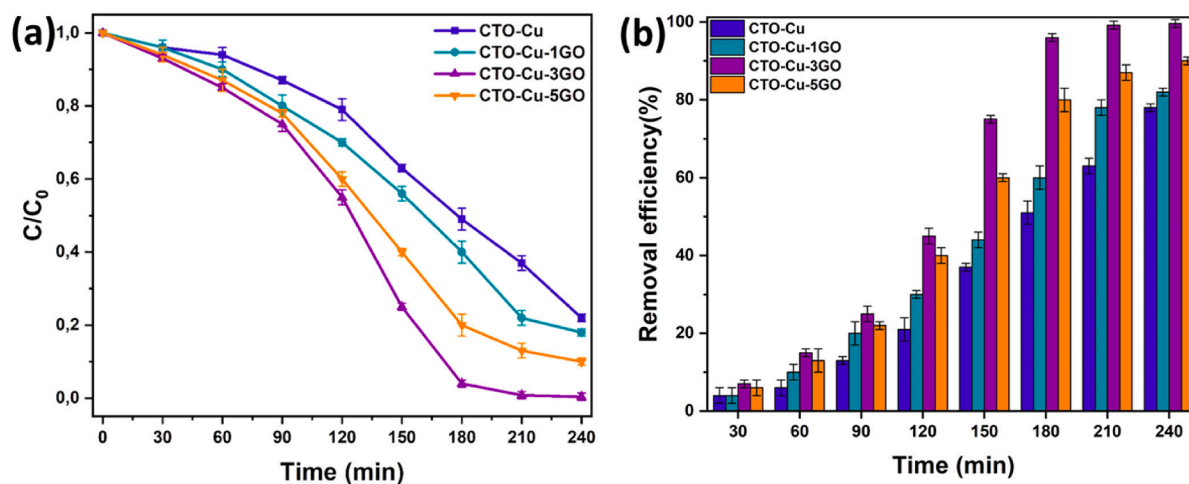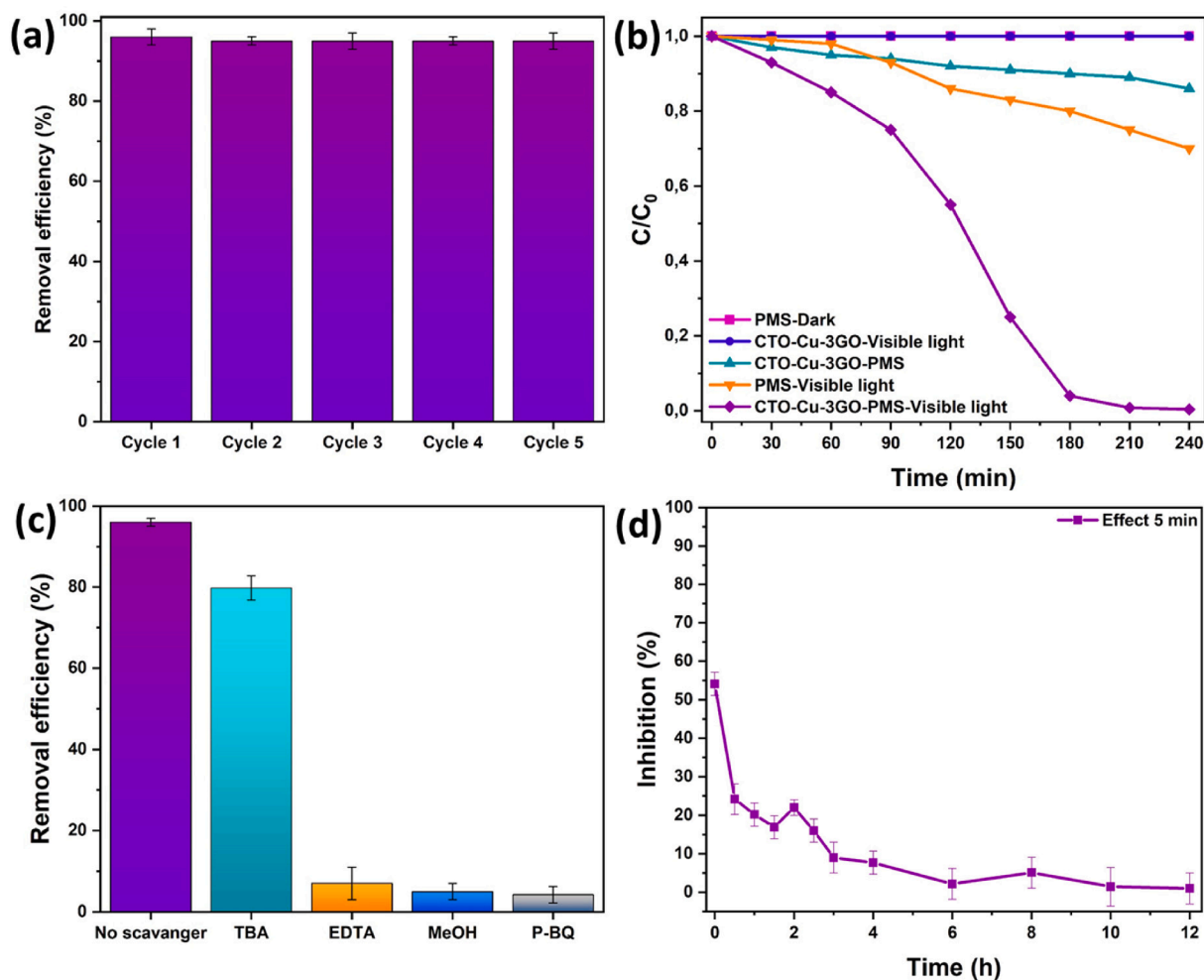

Fig. 6. (a) Normalized concentration decay in function of time for paracetamol photocatalytic degradation (10 ppm) using the indicated pellets under visible light and in the presence of 0.5 mM PMS. (b) Paracetamol removal efficiency.

Fig. 7. (a) CTO-Cu-3GO recycling test. (b) Comparison of paracetamol removal using the indicated conditions. (c) Radical trapping experiments with the indicated scavengers to determine the reactive species implicated in paracetamol degradation in the presence of CTO-Cu-3GO. (d) *Vibrio fischeri* luminescence inhibition (5 min exposure) during paracetamol photocatalytic degradation.

In addition, the catalytic performance was studied by electrochemical impedance spectroscopy to compare the resistance and charge transfer behaviors between fresh and used CTO-Cu-3GO pellets. Fig. S9 shows a slight increase in the semi-circle diameter of the CTO-Cu-3GO-used sample with a little increase in resistance from 438.6 to 477.8 Ohm compared to CTO-Cu-3GO-Fresh. This result confirms that using the sample for 5 degradation cycles did not affect its catalytic properties and the used CTO-Cu-3GO composite materials has strong photochemical stability.

The concern regarding the potential leaching of copper ions after cyclic experiments is indeed a valid one, as it is essential to ensure the environmental safety and long-term stability of the photocatalytic system. To address this concern comprehensively, we conducted a analysis of the copper concentration following five cycles of our photocatalytic process. Therefore, inductively coupled plasma mass spectrometry (Thermo Scientific®, iCAP TQ) was employed for accurate measurements. The result revealed that the leaching concentration of copper after five cycles was exceptionally low, measuring at just 0.01 mg L^{-1}. Additionally, Table S1 indicates that the copper leaching concentration at various time intervals is minimal (0.004–0.008 mg L^{-1}) within the first 120 min and stabilizes at 0.01 after 150 min. This finding underscores the effectiveness of our CTO-Cu-3GO photocatalyst, in retaining copper within the system under visible irradiation. Importantly, this low leaching concentration falls well below established regulatory limits, confirming the environmental safety of our photocatalytic process. This

stability is a key indicator of the material's robustness and its ability to maintain its catalytic performance over extended periods.

Paracetamol mineralization degree was assessed in different conditions to investigate PMS photo-assisted activation with the CTO-Cu-3GO composite. In the PMS-Dark and CTO-Cu-3GO-Visible light conditions, no paracetamol was degraded in 4 h (Fig. 7b), implying that PMS alone cannot degrade paracetamol due to its limited oxidation capacity at ambient temperature [18]. Similarly, CTO-Cu-3GO and visible light were not enough for paracetamol oxidation. In the CTO-Cu-3GO-PMS condition, only 10 % of paracetamol was removed, indicating that the catalyst on its own does not activate PMS. In the presence of PMS and visible light, 20 % of paracetamol was removed, showing that PMS slightly promotes paracetamol photocatalytic degradation. Conversely, the CTO-Cu-3GO-PMS-Visible light condition led to mineralization of 96 % of paracetamol in 3 h, possibly due to the synergistic effect between visible light and CTO-Cu-3GO to promote PMS activation. Indeed, PMS can be activated by visible light irradiation to generate $\cdot SO_4^-$, but with low efficiency. Irradiation of the CTO-Cu-3GO catalyst induces the generation of electron-hole pairs, and the photogenerated electrons can directly activate PMS to produce $\cdot SO_4^-$ radicals [47,91]. Importantly, it has been shown that the key intermediate in PMS activation to generate $\cdot SO_4^-$ is related to the presence of Cu$^+$ in the CTO-Cu-3GO composite [49]. As the XPS results confirmed the presence of Cu^0, Cu$^+$ and Cu^{2+} in this sample, the redox cycling of Cu-based species (Cu^0, Cu$^+$ and Cu^{2+}) plays an essential role in paracetamol degradation [92]. A possible

mechanism may include the following steps: i) Cu^0 oxidation into Cu^+ in the presence of PMS to produce more Cu+ [93]; and ii) Cu^{2+} reduction by PMS and Cu^+ regeneration by the photogenerated electrons [94]. The fast conversion of Cu^{2+} to Cu^+ could be attributed to Cu^0 and the photo-induced electrons. In fact,Cu^0 can act as a reducing agent, facilitating the conversion of Cu^{2+} ions to Cu^+ ions. This reduction process involves the transfer of electrons from Cu^0 to Cu^{2+}, leading to the formation of Cu^+. The Cu^+ ions, which result from the reduction of Cu^{2+}, are known to be active species capable of participating in various redox reactions [50]. All these reactions increase PMS catalytic activity, further promoting paracetamol degradation. Therefore, it is promising to develop TiO_2-$CaTiO_3$-Cu_2O-Cu as a heterogeneous catalyst for PMS activation for use in advanced sulfate radical-based oxidation processes. These composites could be an attractive choice to reduce Cu leaching and prevent secondary contamination, offering an additional beneficial contribution to pollutant removal in the photocatalysis/PMS process. In the realm of mineralization, our focus centers on elucidating the intricate process whereby paracetamol undergoes decomposition. This transformation entails the conversion of paracetamol into smaller compounds, such as short aliphatic chains, through a series of chemical reactions. It is conceivable that this process may culminate in the generation of mineral residues as by-products.

To understand the contribution of reactive species in the mechanism of paracetamol degradation by the CTO-Cu-3GO catalyst, radical trapping experiments were performed using MeOH (trapping reagent for $\cdot SO_4^-$ and $\cdot HO$), TBA (for $\cdot OH$ radicals) [47], and EDTA and p-BQ (for h^+ and $\cdot O_2^-$, respectively) [28,95]. Paracetamol removal efficiency (in the PMS-CTO-Cu-3GO-Visible light condition) decreased from 96 % to less than 10 % after addition of EDTA, MeOH and p-BQ (Fig. 7c), implying that h^+, $\cdot SO_4^-$ and $\cdot O_2^-$ play a dominant role in its photocatalytic degradation. Conversely, TBA addition reduced the removal efficiency only to 80 %, showing that $\cdot OH$ has a minor effect. In fact, the photo-generated holes are indeed pivotal in driving oxidation reactions, particularly in the context of photocatalysis. The quenching of these holes disrupts the delicate redox equilibrium within the photocatalytic system. In this process, the production of strongly reactive species like sulfate or superoxide radicals frequently relies on the presence of photo-generated holes to facilitate the oxidation of water or other precursor molecules. When these holes are quenched, it impedes or completely halts these critical redox reactions, thereby diminishing the system's capacity to efficiently degrade pollutants or accomplish other desired chemical transformations.

Previous studies indicate that some of the intermediate compounds generated in an aqueous environment during paracetamol decomposition may be more harmful than paracetamol [60,96,97]. Therefore, toxicity was studied by measuring *V. fischeri* luminescence inhibition after 5 min of exposure to solutions at different time points of paracetamol degradation. Paracetamol inhibited the luminescence signal by 55 %, but this acute toxicity decreased rapidly during paracetamol degradation to reach 18 % of bioluminescence inhibition after 90 min. Toxicity increased again (24 % of inhibition) after 2 h, suggesting the formation of toxic intermediates, such as p-benzoquinone, benzaldehyde and benzoic acid [62,98,99]. Afterwards, toxicity markedly declined over time as the intermediate products were degraded, and luminescence inhibition reached 0 % after ~ 12 h. These results confirmed that although highly toxic by-products are formed early during paracetamol degradation, they are degraded into less harmful chemicals, such as short-chain carboxylic acids and aromatic compounds, and finally transformed into non-toxic compounds. Furthermore, the findings from the Total Organic Carbon analysis are quite informative. Initially, within the first 2 h, a substantial 40 % reduction in total organic carbon was observed. However, intriguingly, this reduction was maintained stable after 8 h of experimentation. This stabilization can be attributed to the formation of short aliphatic chains as a result of the ongoing chemical processes. It's important to note that despite the transformation of total organic carbon into these shorter aliphatic compounds, there is no cause

for concern regarding toxicity. In fact, the continuous rise in TOC removal signifies the ongoing breakdown of paracetamol into by-products and smaller organic compounds. After two hours, the TOC removal rate peaked at 40 %, indicating the presence of smaller chain aliphatic organic acids—specifically fumaric, oxalic, acetic, and maleic acids—in the solution. This assertion is substantiated by the results of the Microtox test, which unequivocally confirms the absence of toxicity even after a 12-hour assessment period. This outcome underscores the environmentally benign nature of the generated compounds and reinforces the safety of the studied processes. The PMS-CTO-Cu-3GO-Visible light system is relatively environmentally friendly.

Fig. 8 illustrates the potential reaction mechanism for the removal of paracetamol using the CTO-Cu-3GO photocatalyst in the presence of PMS. This model outlines a series of steps that occur during the photo-catalytic process.

In our analysis, diverse references guide the determination of conduction and valence band positions for each component. Specifically, citing source [36], we illustrate the robust reduction capabilities of $CaTiO_3$ and the potent oxidation capabilities of TiO_2 in photocatalytic reactions. This implies that $CaTiO_3$ and TiO_2 serve as the reduction and oxidation zones, respectively. Additionally, referencing source [90], we affirm that the absorption of visible light by the Cu_2O allows efficient transfer of excited electrons from Cu_2O to TiO_2, facilitated by the lower resistance in the copper layer's metal contact, resulting in the generation of holes in the valence band due to the more negative charge of the conduction band of Cu_2O compared to that of TiO_2.

The process begins with the exposure of the photocatalyst, CTO-Cu-3GO, to visible light irradiation. When photons from the light source interact with the photocatalyst, they excite electrons within the material. The absorbed light energy promotes some electrons from their ground state to higher energy levels, creating photoinduced electrons and holes in the photocatalyst. These photoinduced electrons migrate from the conduction band (CB) of Cu_2O to the CBs of other materials in the heterojunction composite, including Cu, TiO_2, and $CaTiO_3$. This migration of electrons is made more efficient by the presence of copper, which has lower resistance compared to other materials. The Cu metal phase in the composite material acts as an electron storage center. As a result, there is a simultaneous presence of photoexcited electrons and holes in both TiO_2 and $CaTiO_3$. On the conduction band (CB) of $CaTiO_3$, there is an abundance of electrons with a high reduction capacity. These electrons can be used in reduction processes to generate $\cdot O_2^-$ radicals, which are reactive oxygen species. The holes generated on the valence band (VB) of Cu_2O have the potential to react with paracetamol pollutants, oxidizing them, or they can produce $\cdot HO$ radicals through the oxidation of water molecules [100,101,36,90]. The transfer of electrons is supported by the generation of reactive oxygen species and the prevention of slow electron-hole recombination [102]. Cu^+ ions, which are formed during the process through the oxidation of Cu^0 and the reduction of Cu^{2+}, have the ability to activate PMS, leading to the production of $\cdot SO_4^-$ radicals [48,94]. All these radicals, including $\cdot O_2^-$, $\cdot HO$, and $\cdot SO_4^-$, participate in the oxidation of paracetamol.

Several types of photocatalysts have been developed and evaluated for the photocatalytic degradation of organic pollutants. Table 4 shows that the CTO-Cu-3GO photocatalyst removal performance is comparable to that of other catalysts reported in the literature.

Upon investigating the effectiveness of our materials in photocatalysis, it becomes fascinating to evaluate how they perform in photoelectrocatalysis for the removal of paracetamol. This investigation will offer valuable insights into potential perspectives, achieved by smoothly combining solar energy and electrical energy. The examination of our materials' dual functionality, capable of utilizing solar power and the applied potential for catalytic reactions, holds promise for innovative and sustainable applications [109].
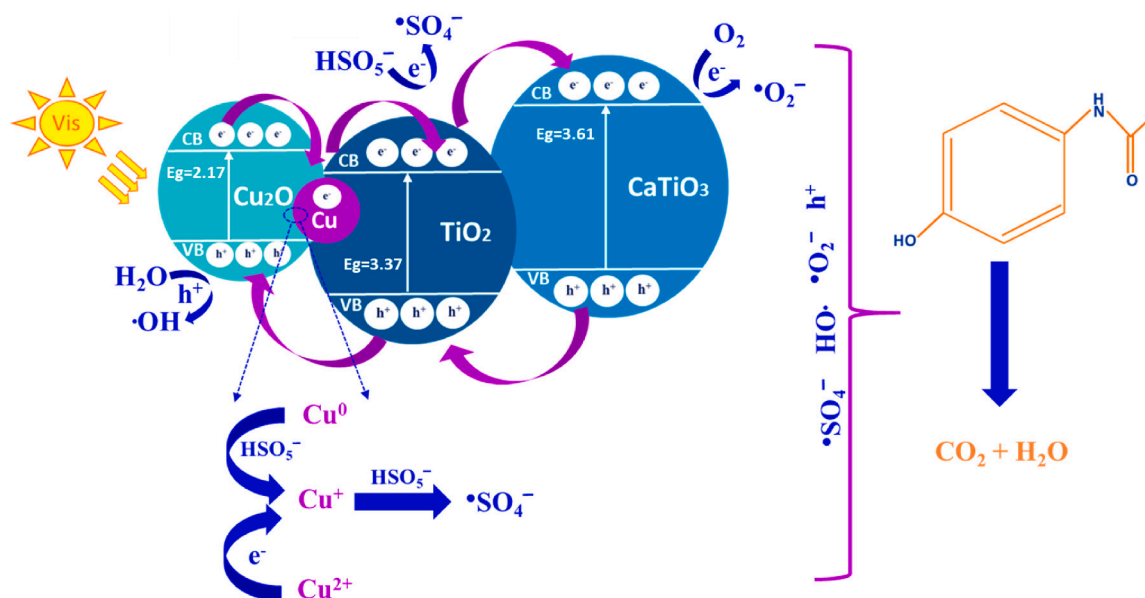
Fig. 8. Mechanism of paracetamol degradation by CTO-Cu-3GO-PMS upon exposure to visible light.

Table 4
Comparative studies on the photocatalytic performance of different composites for the degradation of the indicated organic pollutants.

Pollutant	$C_{pollutant}$ (mg L^{-1})	Photocatalyst	Light source	Solution volume (mL)	Degradation time	Removal efficiency (%)	Ref.
Paracetamol	5	In_2S_3/Zn_2GeO_4	Xenon lamp	100	360	95	[103]
Paracetamol	1	$Cu_2O/WO_3/TiO_2$	150 W Xenon lamp	80	60	92.5	[43]
Paracetamol	10	Pd-BiVO$_4$	300 W Xenon lamp	40	60	100	[104]
Paracetamol	10	B-Bi$_2$O$_3$	1000 W Xenon lamp	50	180	93.6	[105]
Paracetamol	3	g-C$_3$N$_4$-CdS-Bi$_4$O$_5$I$_2$-3	300 W Xenon lamp	50	25	80	[106]
2,20,4,40-tetrabromodiphenyl ether	5	Cu_2O-(rGO -TiO$_2$)	300 W xenon arc lamp	350	180	56	[107]
Tetrabromobisphenol A	10	BiVO$_4$-(rGO-Cu2O)	300 W xenon arc lamp	200	180	90.8	[108]
Paracetamol	10	CTO-Cu-3GO	150 W linear halogen lamp	210	180	96	This work

4. Conclusion

CTO-Cu-GO photocatalysts were successfully synthesized using a solid-state method followed by sintering at 1100 °C in an inert nitrogen atmosphere with different amounts of GO (1, 3, and 5 %) for 3 h. The SEM images showed that the pellet morphologies were well maintained after GO addition. The refinement of XRD data indicated that sintering allowed the formation of TiO$_2$ rutile, CaTiO$_3$, Cu$_2$O and Cu metal phases and that GO presence increased the amount of Cu metal in all composites. The CTO-Cu-3GO composite showed a redshift in the bandgap energy value, confirmed by UV–Vis analysis. The sample with the highest copper amount (CTO-Cu-3GO) displayed good photon absorbance in the visible light region. Electrochemical impedance spectroscopy showed a decrease in the resistance and higher charge separation capacity for the CTO-Cu-3GO catalyst due to the formation of a heterojunction material and transition metal on TiO$_2$. Paracetamol mineralization by photocatalytic degradation was tested in the presence of the fabricated photocatalysts *via* peroxymonosulfate activation under visible light. The highest degradation efficiency (96 %) was reached with the CTO-Cu-3GO sample that displayed high stability (up to five cycles). The mechanistic study showed that Cu$^+$ presence in the catalyst plays a key role in peroxymonosulfate activation. In fact, the composite's combination of multiple semiconductors, including TiO$_2$, CaTiO$_3$, and Cu$_2$O, leads to a synergistic effect, boosting photocatalytic activity. Each constituent plays a role in enhancing light absorption and facilitating charge separation, resulting in more effective paracetamol degradation compared to individual components. Cu$_2$O's capacity to absorb visible light broadens the composite's light spectrum, making it especially advantageous for use in natural sunlight or with low-energy light sources. Heterojunctions formed between TiO$_2$, CaTiO$_3$, Cu$_2$O, and Cu metal further optimize charge separation and movement, ensuring efficient utilization of photo-generated electrons and holes, which reduces electron-hole recombination. The composite's design emphasizes stability and durability, guaranteeing consistent performance over extended durations—essential for practical applications necessitating continuous and reliable paracetamol removal. Its capability to harness visible light, enhance charge separation, generate potent ROS, and offer long-term stability positions it as a valuable solution for addressing pharmaceutical pollutant treatment in water. Overall, the mixing of TiO$_2$ with CTO, Cu$_2$O and Cu metal in the presence of GO is a simple and cheap strategy worth investigating to increase the efficiency of photocatalysts for the mineralization of toxic organic pollutants in wastewater. In the progression of our research, our next step involves merging this advancement of CTO-Cu-GO pellets with a membrane reactor, thereby enabling continuous processing. This transition marks a pivotal phase in our work, with the primary goal being the development of a porous structure that will allow us to simultaneously accomplish two crucial tasks: the filtration and degradation of target substances. This

integrated approach aims to enhance the efficiency and sustainability of our system, paving the way for potentially groundbreaking applications in the fields of water treatment and purification.

CRediT authorship contribution statement

Fida Tanos: Writing – original draft, Validation, Formal analysis, Data curation, Conceptualization. **Elissa Makhoul:** Writing – original draft, Validation, Methodology, Investigation, Formal analysis, Data curation. **Amr Nada:** Writing – original draft, Validation, Investigation, Formal analysis, Data curation. **Maged F. Bekheet:** Writing – review & editing, Validation, Methodology, Formal analysis, Data curation. **Wiebke Riedel:** Writing – review & editing, Validation, Formal analysis, Data curation. **Sarah Kawrani:** Writing – review & editing, Validation, Formal analysis, Data curation. **Habib Belaid:** Writing – review & editing, Validation, Formal analysis, Data curation. **Eddy Petit:** Writing – review & editing, Validation, Formal analysis, Data curation. **Roman Viter:** Writing – original draft, Resources, Methodology, Funding acquisition, Formal analysis, Data curation. **Victoriia Fedorenko:** Writing – review & editing, Validation, Formal analysis, Data curation. **Arunas Ramanavicius:** Writing – review & editing, Supervision, Methodology, Formal analysis. **Madona Boulos:** Writing – review & editing, Supervision, Methodology, Funding acquisition. **David Cornu:** Writing – review & editing, Supervision, Methodology, Formal analysis. **Antonio Razzouk:** Writing – review & editing, Supervision, Resources. **Geoffroy Lesage:** Writing – review & editing, Validation, Supervision, Resources, Formal analysis. **Marc Cretin:** Writing – review & editing, Validation, Supervision, Methodology, Formal analysis. **Mikhael Bechelany:** Writing – review & editing, Validation, Supervision, Resources, Project administration, Methodology, Conceptualization.

Declaration of competing interest

The authors declare that they have no known competing financial interests or personal relationships that could have appeared to influence the work reported in this paper.

Data availability

Data will be made available on request.

Acknowledgements

Appendix A. Supplementary data

Supplementary data to this article can be found online at https://doi. org/10.1016/j.apsusc.2024.159698.

References

[1] K.S. Varma, R.J. Tayade, K.J. Shah, P.A. Joshi, A.D. Shukla, V.G. Gandhi, Photocatalytic degradation of pharmaceutical and pesticide compounds (ppcs) using doped tio2 nanomaterials: a review, Water-Energy Nexus 3 (2020) 46–61, https://doi.org/10.1016/j.wen.2020.03.008.

[2] H.S. Kushwaha, P. Thomas, R. Vaish, Polyaniline/CaCu$_3$Ti$_4$O$_{12}$ nanofiber composite with a synergistic effect on visible light photocatalysis, RSC Adv. 5 (106) (2015) 87241–87250, https://doi.org/10.1039/C5RA16518K.

[3] R. Hailili, Z.-Q. Wang, Y. Li, Y. Wang, V.K. Sharma, X.-Q. Gong, C. Wang, Oxygen vacancies induced visible-light photocatalytic activities of cacu3ti4o12 with

controllable morphologies for antibiotic degradation, Appl. Catal. B Environ. 221 (2018) 422–432, https://doi.org/10.1016/j.apcatb.2017.09.026.

[4] J. Rivera-Utrilla, M. Sánchez-Polo, M.Á. Ferro-García, G. Prados-Joya, R. Ocampo-Pérez, Pharmaceuticals as emerging contaminants and their removal from water, A Review. *Chemosphere* 93 (7) (2013) 1268–1287, https://doi.org/10.1016/j.chemosphere.2013.07.059.

[5] L. Lin, W. Jiang, M. Bechelany, M. Nasr, J. Jarvis, T. Schaub, R.R. Sapkota, P. Miele, H. Wang, P. Xu, Adsorption and photocatalytic oxidation of ibuprofen using nanocomposites of tio2 nanofibers combined with bn nanosheets: degradation products and mechanisms, Chemosphere 220 (2019) 921–929, https://doi.org/10.1016/j.chemosphere.2018.12.184.

[6] I. Ali, V.K. Gupta, Advances in water treatment by adsorption technology, Nat. Protoc. 1 (6) (2006) 2661–2667, https://doi.org/10.1038/nprot.2006.370.

[7] S.K. Fanourakis, J. Peña-Bahamonde, P.C. Bandara, D.F. Rodrigues, Nano-based adsorbent and photocatalyst use for pharmaceutical contaminant removal during indirect potable water reuse, Npj Clean Water 3 (1) (2020) 1, https://doi.org/10.1038/s41545-019-0048-8.

[8] B.O. Orimolade, O.A. Arotiba, An exfoliated graphite-bismuth vanadate composite photoanode for the photoelectrochemical degradation of acid orange 7 dye, Electrocatalysis 10 (4) (2019) 429–435, https://doi.org/10.1007/s12678-019-00534-5.

[9] Y. Tian, N. Jia, L. Zhou, J. Lei, L. Wang, J. Zhang, Y. Liu, Photo-fenton-like degradation of antibiotics by inverse opal wo3 co-catalytic fe2+/pms, fe2+/h2o2 and fe2+/pds processes: a comparative study, Chemosphere 288 (2022) 132627, https://doi.org/10.1016/j.chemosphere.2021.132627.

[10] M.G. Peleyeju, O.A. Arotiba, Recent trend in visible-light photoelectrocatalytic systems for degradation of organic contaminants in water/wastewater, Environ. Sci. Water Res. Technol. 4 (10) (2018) 1389–1411, https://doi.org/10.1039/C8EW00276B.

[11] X. Jiang, L. Huang, L. Zhang, J. Li, X. Sun, N-doped cotton-based porous carbon/zno nr arrays: highly efficient hybrid photo-catalysts, CrystEngComm 22 (14) (2020) 2472–2482, https://doi.org/10.1039/D0CE00222D.

[12] T.X.H. Le, M. Bechelany, S. Lacour, N. Oturan, M.A. Oturan, M. Cretin, High removal efficiency of dye pollutants by electron-fenton process using a graphene based cathode, Carbon 94 (2015) 1003–1011, https://doi.org/10.1016/j.carbon.2015.07.086.

[13] S.O. Ganiyu, S. Sable, M. Gamal El-Din, Advanced oxidation processes for the degradation of dissolved organics in produced water: a review of process performance, degradation kinetics and pathway, Chem. Eng. J. 429 (2022) 132492, https://doi.org/10.1016/j.cej.2021.132492.

[14] Y.M. Hunge, A.A. Yadav, S.-W. Kang, H. Kim, Photocatalytic degradation of tetracycline antibiotics using hydrothermally synthesized two-dimensional molybdenum disulfide/titanium dioxide composites, J. Colloid Interface Sci. 606 (2022) 454–463, https://doi.org/10.1016/j.jcis.2021.07.151.

[15] M. Nasr, C. Eid, R. Habchi, P. Miele, M. Bechelany, Recent progress on titanium dioxide nanomaterials for photocatalytic applications, ChemSusChem 11 (18) (2018) 3023–3047, https://doi.org/10.1002/cssc.201800874.

[16] M. Nasr, R. Viter, C. Eid, R. Habchi, P. Miele, M. Bechelany, Enhanced photocatalytic performance of novel electrospun bn/tio2 composite nanofibers, New J. Chem. 41 (2017) 81–89.

[17] A.A. Nada, H.R. Tantawy, M.A. Elsayed, M. Bechelany, M.E. Elmowafy, Elaboration of nano titania-magnetic reduced graphene oxide for degradation of tartrazine dye in aqueous solution, Solid State Sci. 78 (2018) 116–125, https://doi.org/10.1016/j.solidstatesciences.2018.02.014.

[18] Q. Zhang, X. Sun, Y. Dang, J.-J. Zhu, Y. Zhao, X. Xu, Y. Zhou, A novel electrochemically enhanced homogeneous pms-heterogeneous cofe2o4 synergistic catalysis for the efficient removal of levofloxacin, J. Hazard. Mater. 424 (2022) 127651, https://doi.org/10.1016/j.jhazmat.2021.127651.

[19] M. Noorisepehr, B. Kakavandi, A.A. Isari, F. Ghanbari, E. Dehghanifard, N. Ghomi, F. Kamrani, Sulfate radical-based oxidative degradation of acetaminophen over an efficient hybrid system: peroxydisulfate decomposed by ferroferric oxide nanocatalyst anchored on activated carbon and uv light, Sep. Purif. Technol. 250 (2020) 116950, https://doi.org/10.1016/j.seppur.2020.116950.

[20] J.M. Dangwang Dikdim, Y. Gong, G.B. Noumi, J.M. Sieliechi, X. Zhao, N. Ma, M. Yang, J.B. Tchatchueng, Peroxymonosulfate improved photocatalytic degradation of atrazine by activated carbon/graphitic carbon nitride composite under visible light irradiation, Chemosphere 217 (2019) 833–842, https://doi.org/10.1016/j.chemosphere.2018.10.177.

[21] X. Li, B. Jie, H. Lin, Z. Deng, J. Qian, Y. Yang, X. Zhang, Application of sulfate radicals-based advanced oxidation technology in degradation of trace organic contaminants (trocs): recent advances and prospects, J. Environ. Manage. 308 (2022) 114664, https://doi.org/10.1016/j.jenvman.2022.114664.

[22] X. Duan, S. Yang, S. Wacławek, G. Fang, R. Xiao, D.D. Dionysiou, Limitations and prospects of sulfate-radical based advanced oxidation processes, J. Environ. Chem. Eng. 8 (4) (2020) 103849, https://doi.org/10.1016/j.jece.2020.103849.

[23] X. Zheng, X. Niu, D. Zhang, M. Lv, X. Ye, J. Ma, Z. Lin, M. Fu, Metal-based catalysts for persulfate and peroxymonosulfate activation in heterogeneous ways: a review, Chem. Eng. J. 429 (2022) 132323, https://doi.org/10.1016/j.cej.2021.132323.

[24] R. Tang, D. Gong, Y. Deng, S. Xiong, J. Deng, L. Li, Z. Zhou, J. Zheng, L. Su, L. Yang, π-π stacked step-scheme pdi/g-c3n4/tio2@ti3c2 photocatalyst with enhanced visible photocatalytic degradation towards atrazine via peroxymonosulfate activation, Chem. Eng. J. 427 (2022) 131809, https://doi.org/10.1016/j.cej.2021.131809.

[25] F. Liu, Q. Dong, C. Nie, Z. Li, B. Zhang, P. Han, W. Yang, M. Tong, Peroxymonosulfate enhanced photocatalytic degradation of serial bisphenols by metal-free covalent organic frameworks under visible light irradiation: mechanisms, degradation pathway and dft calculation, Chem. Eng. J. 430 (2022) 132833, https://doi.org/10.1016/j.cej.2021.132833.

[26] S. Li, Y. Yang, H. Zheng, Y. Zheng, T. Jing, J. Ma, J. Nan, Y.K. Leong, J.-S. Chang, Advanced Oxidation process based on hydroxyl and sulfate radicals to degrade refractory organic pollutants in landfill leachate, Chemosphere 297 (2022) 134214, https://doi.org/10.1016/j.chemosphere.2022.134214.

[27] A.A. Nada, W.M.A. El Rouby, M.F. Bekheet, M. Antuch, M. Weber, P. Miele, R. Viter, S. Roualdes, P. Millet, M. Bechelany, Highly textured boron/nitrogen co-doped tio2 with honeycomb structure showing enhanced visible-light photoelectrocatalytic activity, Appl. Surf. Sci. 505 (2020) 144419, https://doi.org/10.1016/j.apsusc.2019.144419.

[28] Sayegh, S.; Tanos, F.; Nada, A.; Lesage, G.; Zaviska, F.; Petit, E.; Rouessac, V.; Iatsunskyi, I.; Coy, E.; Viter, R.; Damberga, D.; Weber, M.; Razzouk, A.; Stephan, J.; Bechelany, M. Tunable TiO$_2$ –BN–Pd Nanofibers by Combining Electrospinning and Atomic Layer Deposition to Enhance Photodegradation of Acetaminophen. *Dalton Trans.* **2022**, 10.1039.D1DT03715C. 10.1039/D1DT03715C.

[29] M. Nasr, S. Balme, C. Eid, R. Habchi, P. Miele, M. Bechelany, Enhanced visible-light photocatalytic performance of electrospun rgo/tio$_2$ composite nanofibers, J. Phys. Chem. C 121 (1) (2017) 261–269, https://doi.org/10.1021/acs.jpcc.6b08840.

[30] S. Ramanavicius, A. Ramanavicius, Insights in the application of stoichiometric and non-stoichiometric titanium oxides for the design of sensors for the determination of gases and VOCs (TiO2−x and TinO2n−1 vs, TiO2). Sensors 20 (23) (2020) 6833, https://doi.org/10.3390/s20236833.

[31] E. Coy, K. Siuzdak, M. Pavlenko, K. Załęski, O. Graniel, M. Ziółek, S. Balme, P. Miele, M. Weber, M. Bechelany, I. Iatsunskyi, Enhancing photocatalytic performance and solar absorption by schottky nanodiodes heterojunctions in mechanically resilient palladium coated tio2/si nanopillars by atomic layer deposition, Chem. Eng. J. 392 (2020) 123702, https://doi.org/10.1016/j.cej.2019.123702.

[32] L. Lin, W. Jiang, M. Nasr, M. Bechelany, P. Miele, H. Wang, P. Xu, Enhanced visible light photocatalysis by tio$_2$ –bn enabled electrospinning of nanofibers for pharmaceutical degradation and wastewater treatment, Photochem. Photobiol. Sci. 18 (12) (2019) 2921–2930, https://doi.org/10.1039/C9PP00304E.

[33] M. Shi, B. Rhimi, K. Zhang, J. Xu, D.W. Bahnemann, C. Wang, Visible light-driven novel bi2ti2o7/catio3 composite photocatalyst with enhanced photocatalytic activity towards no removal, Chemosphere 275 (2021) 130083, https://doi.org/10.1016/j.chemosphere.2021.130083.

[34] N. Li, M. Shi, Y. Xin, W. Zhang, J. Qin, K. Zhang, H. Lv, M. Yuan, C. Wang, Oxygen vacancies-modified s-scheme bi2ti2o7/catio3 heterojunction for highly efficient photocatalytic no removal under visible light, J. Environ. Chem. Eng. 10 (3) (2022) 107420, https://doi.org/10.1016/j.jece.2022.107420.

[35] S. Balachandran, M. Swaminathan, Facile fabrication of heterostructured bi$_2$o$_3$ –zno photocatalyst and its enhanced photocatalytic activity, J. Phys. Chem. C 116 (50) (2012) 26306–26312, https://doi.org/10.1021/jp306874z.

[36] J. Yang, C. Shi, Y. Dong, H. Su, H. Sun, Y. Guo, S. Yin, Efficient hydrogen generation of vector z-scheme catio3/cu/tio2 photocatalyst assisted by cocatalyst cu nanoparticles, J. Colloid Interface Sci. 605 (2022) 373–384, https://doi.org/10.1016/j.jcis.2021.07.106.

[37] X. Gao, M. Song, D. Sun, R. Guan, H. Zhai, Z. Zhao, Q. Zhang, X. Li, A facile in situ hydrothermal etching method to catio3/tio2 heterostructure for efficient photocatalytic n2 reduction, Catal. Lett. (2021), https://doi.org/10.1007/s10562-021-03813-3.

[38] J. Lin, J. Hu, C. Qiu, H. Huang, L. Chen, Y. Xie, Z. Zhang, H. Lin, X. Wang, *In Situ* hydrothermal etching fabrication of CaTiO$_3$ on TiO$_2$ nanosheets with heterojunction effects to enhance CO$_2$ adsorption and photocatalytic Reduction, Catal. Sci. Technol. 9 (2) (2019) 336–346, https://doi.org/10.1039/C8CY02142B.

[39] B. Babu, A.N. Kadam, R.V.S.S.N. Ravikumar, C. Byon, Enhanced visible light photocatalytic activity of cu-doped sno2 quantum dots by solution combustion synthesis, J. Alloys Compd. 703 (2017) 330–336, https://doi.org/10.1016/j.jallcom.2017.01.311.

[40] C. Li, T. Sun, D. Zhang, X. Zhang, Y. Qian, Y. Zhang, X. Lin, J. Liu, L. Zhu, X. Wang, Z. Shi, Q. Lin, Fabrication of ternary ag/la-black tio2−x photocatalyst with enhanced visible-light photocatalytic activity for tetracycline degradation, J. Alloys Compd. 891 (2022) 161960, https://doi.org/10.1016/j.jallcom.2021.161960.

[41] S. Wannapop, A. Somdee, Highly orientated one-dimensional cu2o/tio2 heterostructure thin film for photoelectrochemical photoanode and photocatalytic degradation applications, Thin Solid Films 747 (2022) 139144, https://doi.org/10.1016/j.tsf.2022.139144.

[42] M.S. Mahmoud, E. Ahmed, A.A. Farghali, A.H. Zaki, E.A.M. Abdelghani, N.A. M. Barakat, Influence of Mn, Cu, and Cd–Doping for titanium oxide nanotubes on the photocatalytic activity toward water splitting under visible light irradiation, Colloids Surf. Physicochem. Eng. Asp. 554 (2018) 100–109, https://doi.org/10.1016/j.colsurfa.2018.06.039.

[43] J.H.F. Chau, C.W. Lai, B.F. Leo, J.C. Juan, M.R. Johan, Advanced photocatalytic degradation of acetaminophen using cu2o/wo3/tio2 ternary composite under solar irradiation, Catal. Commun. 163 (2022) 106396, https://doi.org/10.1016/j.catcom.2022.106396.

[44] A.L.T. Zheng, S. Sabidi, T. Ohno, T. Maeda, Y. Andou, Cu2O/TiO2 decorated on cellulose nanofiber/reduced graphene hydrogel for enhanced photocatalytic

[45] C. Garlisi, J. Szlachetko, C. Aubry, D.L.A. Fernandes, Y. Hattori, C. Paun, M. V. Pavliuk, N.S. Rajput, E. Lewin, J. Sá, G. Palmisano, N-TiO2/Cu-TiO2 double-layer films: impact of stacking order on photocatalytic properties, J. Catal. 353 (2017) 116–122, https://doi.org/10.1016/j.jcat.2017.06.028.

[46] S. Rtimi, S. Giannakis, R. Sanjines, C. Pulgarin, M. Bensimon, J. Kiwi, Insight on the Photocatalytic bacterial inactivation by co-sputtered tio 2 –cu in aerobic and anaerobic conditions, Appl. Catal. B Environ. 182 (2016) 277–285, https://doi.org/10.1016/j.apcatb.2015.09.041.

[47] Y. Huang, J. Li, P. Du, X. Lu, Rational design of copper encapsulated within nitrogen-doped carbon core-shell nanosphere for efficiently photocatalytic peroxymonosulfate activation, J. Colloid Interface Sci. 597 (2021) 206–214, https://doi.org/10.1016/j.jcis.2021.04.016.

[48] L. Zhang, Y. Wang, R. Djellabi, Y. Wang, J. Zhao, X. Zhao, Simultaneous oxidation of 2,4-dichlorophenol and cu deposition over cuprous phosphide-doped carbon aerogel in the presence of peroxymonosulfate, Sep. Purif. Technol. 288 (2022) 120671, https://doi.org/10.1016/j.seppur.2022.120671.

[49] Y. Zhu, T. Wang, W. Wang, S. Chen, E. Lichtfouse, C. Cheng, J. Zhao, Y. Li, C. Wang, CaCu3Ti4O12, an efficient catalyst for ibuprofen removal by activation of peroxymonosulfate under visible-light irradiation, Environ. Chem. Lett. 17 (1) (2019) 481–486, https://doi.org/10.1007/s10311-018-0776-x.

[50] B. Wang, T. Fu, B. An, Y. Liu, UV light-assisted persulfate activation by cu0-cu2o for the degradation of sulfamerazine, Sep. Purif. Technol. 251 (2020) 117321, https://doi.org/10.1016/j.seppur.2020.117321.

[51] R.K. Upadhyay, N. Soin, S.S. Roy, Role of graphene/metal oxide composites as photocatalysts, adsorbents and disinfectants in water treatment: a review, RSC Adv 4 (8) (2014) 3823–3851, https://doi.org/10.1039/C3RA45013A.

[52] N. Singh, J. Prakash, R.K. Gupta, Design and engineering of high-performance photocatalytic systems based on metal oxide–graphene–noble metal nanocomposites, Mol. Syst. Des. Eng. 2 (4) (2017) 422–439, https://doi.org/10.1039/C7ME00038C.

[53] L. Li, J. Zhang, X. Fu, P. Xiao, M. Zhang, M. Liu, One-pot solid-state reaction approach to synthesize ag-cu$_2$o/go ternary nanocomposites with enhanced visible-light-responsive photocatalytic activity, Int. J. Photoenergy 2017 (2017) 1–8, https://doi.org/10.1155/2017/8983717.

[54] H. Fan, X. Zhao, J. Yang, X. Shan, L. Yang, Y. Zhang, X. Li, M. Gao, ZnO–Graphene composite for photocatalytic degradation of methylene blue dye, Catal. Commun. 29 (2012) 29–34, https://doi.org/10.1016/j.catcom.2012.09.013.

[55] S. Kawrani, M. Boulos, M.F. Bekheet, R. Viter, A.A. Nada, W. Riedel, S. Roualdes, D. Cornu, M. Bechelany, Segregation of copper oxide on calcium copper titanate surface induced by graphene oxide for water splitting applications, Appl. Surf. Sci. 516 (2020) 146051, https://doi.org/10.1016/j.apsusc.2020.146051.

[56] H. Belaid, S. Nagarajan, C. Teyssier, C. Barou, J. Barés, S. Balme, H. Garay, V. Huon, D. Cornu, V. Cavaillès, M. Bechelany, Development of new biocompatible 3d printed graphene oxide-based scaffolds, Mater. Sci. Eng. C 110 (2020) 110595, https://doi.org/10.1016/j.msec.2019.110595.

[57] J. Rodriguez-Carvajal, Recent developments of the program fullprof, commission on powder diffraction, Iucr Newsl 26 (2001).

[58] L. Finger, D. Cox, A. Jephcoat, A correction for powder diffraction peak asymmetry due to axial divergence, J. Appl. Crystallogr. 27 (1994) 892–900, https://doi.org/10.1107/S0021889894004218.

[59] M. Hosseini, A. Esrafili, M. Farzadkia, M. Kermani, M. Gholami, Degradation of Ciprofloxacin Antibiotic Using Photo-Electrocatalyst Process of Ni-Doped ZnO Deposited by RF Sputtering on FTO as an Anode Electrode from Aquatic Environments: Synthesis, Kinetics, and Ecotoxicity Study, Microchem. J. 154 (2020) 104663, https://doi.org/10.1016/j.microc.2020.104663.

[60] B.O. Orimolade, B.N. Zwane, B.A. Koiki, M. Rivallin, M. Bechelany, N. Mabuba, G. Lesage, M. Cretin, O.A. Arotiba, Coupling cathodic electro-fenton with anodic photo-electrochemical oxidation: a feasibility study on the mineralization of paracetamol, J. Environ. Chem. Eng. 8 (5) (2020) 104394, https://doi.org/10.1016/j.jece.2020.104394.

[61] T.X.H. Le, T.V. Nguyen, Z.A. Yacouba, L. Zoungrana, F. Avril, E. Petit, J. Mendret, V. Bonniol, M. Bechelany, S. Lacour, G. Lesage, M. Cretin, Toxicity removal assessments related to degradation pathways of azo dyes: toward an optimization of electro-fenton treatment, Chemosphere 161 (2016) 308–318, https://doi.org/10.1016/j.chemosphere.2016.06.108.

[62] T.X.H. Le, T.V. Nguyen, Z. Amadou Yacouba, L. Zoungrana, F. Avril, D.L. Nguyen, E. Petit, J. Mendret, V. Bonniol, M. Bechelany, S. Lacour, G. Lesage, M. Cretin, Correlation between degradation pathway and toxicity of acetaminophen and its by-products by using the electro-fenton process in aqueous media, Chemosphere 172 (2017) 1–9, https://doi.org/10.1016/j.chemosphere.2016.12.060.

[63] M.F. Bekheet, M. Miehe, C. Fasel, A. Gurlo, R. Riedel, Low temperature synthesis of nanocrystalline mnin2o4 spinel, Dalton Trans. 41 (12) (2012) 3374, https://doi.org/10.1039/c2dt12473d.

[64] M.F. Bekheet, L. Schlicker, A. Doran, K. Siemensmeyer, A. Gurlo, Ferrimagnetism in manganese-rich gallium and aluminium spinels due to mixed valence Mn 2+ –Mn 3+ States, Dalton Trans. 47 (8) (2018) 2727–2738, https://doi.org/10.1039/C7DT04765G.

[65] A. Bartoletti, A. Gondolini, E. Sangiorgi, M. Aramini, M. Ardit, M. Rancan, L. Armelao, S.A. Kondrat, A. Sanson, Identification of structural changes in cacu$_3$ ti$_4$o$_{12}$ on high energy ball milling and their effect on photocatalytic performance, Catal. Sci. Technol. 13 (4) (2023) 1041–1058, https://doi.org/10.1039/D2CY01299E.

[66] Y. Wang, L. Li, X. Huang, Q. Li, G. Li, New insights into fluorinated tio 2 (brookite, anatase and rutile) nanoparticles as efficient photocatalytic redox

catalysts, RSC Adv. 5 (43) (2015) 34302–34313, https://doi.org/10.1039/C4RA17076H.

[67] C. Rani, D.K. Pathak, M. Tanwar, S. Kandpal, T. Ghosh, M.Y. Maximov, R. Kumar, Anharmonicity induced faster decay of hot phonons in rutile tio $_2$ nanorods: a raman spectromicroscopy study, Mater. Adv. 3 (3) (2022) 1602–1608, https://doi.org/10.1039/D1MA00940K.

[68] V. Swamy, B.C. Muddle, Q. Dai, Size-dependent modifications of the raman spectrum of rutile TiO2, Appl. Phys. Lett. 89 (16) (2006) 163118, https://doi.org/10.1063/1.2364123.

[69] A. Romero-Morán, A. Zavala-Franco, J.L. Sánchez-Salas, M.Á. Méndez-Rojas, J. Molina-Reyes, Electrostatically charged rutile tio2 surfaces with enhanced photocatalytic activity for bacteria inactivation, Catal. Today 392–393 (2022) 154–166, https://doi.org/10.1016/j.cattod.2022.01.002.

[70] S. Kawrani, A.A. Nada, M.F. Bekheet, M. Boulos, R. Viter, S. Roualdes, P. Miele, D. Cornu, M. Bechelany, Enhancement of calcium copper titanium oxide photoelectrochemical performance using boron nitride nanosheets, Chem. Eng. J. 389 (2020) 124326, https://doi.org/10.1016/j.cej.2020.124326.

[71] D. Das, P. Makal, Narrow band gap reduced tio2-b: cu nanowire heterostructures for efficient visible light absorption, charge separation and photocatalytic degradation, Appl. Surf. Sci. 506 (2020) 144880, https://doi.org/10.1016/j.apsusc.2019.144880.

[72] Q. Zhang, L. Huang, S. Kang, C. Yin, Z. Ma, L. Cui, Y. Wang, CuO/Cu $_2$ O nanowire arrays grafted by reduced graphene oxide: synthesis, characterization, and application in photocatalytic reduction of CO $_2$, RSC Adv. 7 (69) (2017) 43642–43647, https://doi.org/10.1039/C7RA07310K.

[73] D. Li, G. Wang, L. Cheng, C. Wang, X. Mei, Engineering the self-assembly induced emission of copper nanoclusters as 3d nanomaterials with mesoporous sphere structures by the crosslinking of Ce ^{3}+, ACS Omega 3 (11) (2018) 14755–14765, https://doi.org/10.1021/acsomega.8b02204.

[74] C. Cheng, C. Zhang, X. Gao, Z. Zhuang, C. Du, W. Chen, 3D network and 2d paper of reduced graphene oxide/cu $_2$ o composite for electrochemical sensing of hydrogen peroxide, Anal. Chem. 90 (3) (2018) 1983–1991, https://doi.org/10.1021/acs.analchem.7b04070.

[75] Q. Wang, Y. Zhang, Y. Liu, K. Wang, W. Qiu, L. Chen, W. Li, J. Li, Photocorrosion behavior of cu2o nanowires during photoelectrochemical co2 reduction, J. Electroanal. Chem. 912 (2022) 116252, https://doi.org/10.1016/j.jelechem.2022.116252.

[76] R.C. Pawar, D.-H. Choi, J.-S. Lee, C.S. Lee, Formation of polar surfaces in microstructured zno by doping with cu and applications in photocatalysis using visible light, Mater. Chem. Phys. 151 (2015) 167–180, https://doi.org/10.1016/j.matchemphys.2014.11.051.

[77] Z. Gu, N. Yang, P. Han, M. Kuang, B. Mei, Z. Jiang, J. Zhong, L. Li, G. Zheng, Oxygen vacancy tuning toward efficient electrocatalytic co $_2$ reduction to C $_2$ H $_4$, Small Methods 1800449 (2018), https://doi.org/10.1002/smtd.201800449.

[78] H. Zhang, G. Zhang, Z. Li, K. Qu, L. Wang, W. Zeng, Q. Zhang, H. Duan, Ultra-uniform cuo/cu in nitrogen-doped carbon nanofibers as a stable anode for li-ion batteries, J. Mater. Chem. A 4 (27) (2016) 10585–10592, https://doi.org/10.1039/C6TA02875F.

[79] H.H. El-Maghrabi, A.A. Nada, S. Roualdes, M.F. Bekheet, Design of Ni/NiO-TiO2/RGO nanocomposites on carbon cloth conductors via pecvd for electrocatalytic water splitting, Int. J. Hydrog. Energy 45 (56) (2020) 32000–32011, https://doi.org/10.1016/j.ijhydene.2020.08.259.

[80] F. Peng, L. Cai, H. Yu, H. Wang, J. Yang, Synthesis and characterization of substitutional and interstitial nitrogen-doped titanium dioxides with visible light photocatalytic activity, J. Solid State Chem. 181 (1) (2008) 130–136, https://doi.org/10.1016/j.jssc.2007.11.012.

[81] L.S. Yoong, F.K. Chong, B.K. Dutta, Development of copper-doped tio2 photocatalyst for hydrogen production under visible light, Energy 34 (10) (2009) 1652–1661, https://doi.org/10.1016/j.energy.2009.07.024.

[82] M.M. Momeni, Y. Ghayeb, Z. Ghonchegi, Fabrication and characterization of copper doped tio2 nanotube arrays by in situ electrochemical method as efficient visible-light photocatalyst, Ceram. Int. 41 (7) (2015) 8735–8741, https://doi.org/10.1016/j.ceramint.2015.03.094.

[83] S.P. Takle, O.A. Apine, D.B. Bankar, A.S. Tarlekar, N.N. Bhujbal, B.B. Kale, R.S. Sonawane, Sunlight mediated degradation of spent wash using hydrothermally synthesized orthorhombic shaped cu–tio $_2$ nanoparticles, New J. Chem. 44 (41) (2020) 17724–17734, https://doi.org/10.1039/D0NJ03309J.

[84] Nguyen Thi Thu, T.; Nguyen Thi, N.; Tran Quang, V.; Nguyen Hong, K.; Nguyen Minh, T.; Le Thi Hoai, N. Synthesis, Characterisation, and Effect of PH on Degradation of Dyes of Copper-Doped TiO 2. J. Exp. Nanosci. 2016, 11 (3), 226–238. 10.1080/17458080.2015.1053541.

[85] T. Raguram, K.S. Rajni, Synthesis and characterisation of cu - doped tio2 nanoparticles for dssc and photocatalytic applications, Int. J. Hydrog. Energy 47 (7) (2022) 4674–4689, https://doi.org/10.1016/j.ijhydene.2021.11.113.

[86] B.O. Orimolade, B.A. Koiki, G.M. Peleyeju, O.A. Arotiba, Visible light driven photoelectrocatalysis on a fto/bivo4/bioi anode for water treatment involving emerging pharmaceutical pollutants, Electrochimica Acta 307 (2019) 285–292, https://doi.org/10.1016/j.electacta.2019.03.217.

[87] J. Zhong, J. Huang, Y. Liu, D. Li, C. Tan, P. Chen, H. Liu, X. Zheng, C. Wen, W. Lv, G. Liu, Construction of double-functionalized g-c3n4 heterojunction structure via optimized charge transfer for the synergistically enhanced photocatalytic degradation of sulfonamides and h2o2 production, J. Hazard. Mater. 422 (2022) 126868, https://doi.org/10.1016/j.jhazmat.2021.126868.

[88] G. Huang, W. Ye, C. Lv, D.S. Butenko, C. Yang, G. Zhang, P. Lu, Y. Xu, S. Zhang, H. Wang, Y. Zhu, D. Yang, Hierarchical red phosphorus incorporated tio2 hollow sphere heterojunctions toward superior photocatalytic hydrogen production,

[89] P. Qiu, Y. Zhang, G. Cheng, Precursor self-derived cu@tio2 hybrid schottky junction for enhanced solar-to-hydrogen evolution, Int. J. Hydrog. Energy 47 (19) (2022) 10628–10637, https://doi.org/10.1016/j.ijhydene.2022.01.113.

[90] Z. Li, J. Liu, D. Wang, Y. Gao, J. Shen, Cu2O/Cu/TiO2 nanotube ohmic heterojunction arrays with enhanced photocatalytic hydrogen production activity, Int. J. Hydrog. Energy 37 (8) (2012) 6431–6437, https://doi.org/10.1016/j.ijhydene.2012.01.075.

[91] T. Guo, L. Jiang, H. Huang, Y. Li, X. Wu, G. Zhang, Enhanced degradation of tetracycline in water over cu-doped hematite nanoplates by peroxymonosulfate activation under visible light irradiation, J. Hazard. Mater. 416 (2021) 125838, https://doi.org/10.1016/j.jhazmat.2021.125838.

[92] X. Mi, H. Zhong, H. Zhang, S. Xu, Y. Li, H. Wang, S. Zhan, J.C. Crittenden, Facilitating redox cycles of copper species by pollutants in peroxymonosulfate activation, Environ. Sci. Technol. 56 (4) (2022) 2637–2646, https://doi.org/10.1021/acs.est.1c06762.

[93] Y. Zhang, Y. Wang, X. Zhang, L. Wu, H. Wang, X. Wei, W.D. Wu, X. Wang, W. Li, Z. Wu, Microdroplet confined assembly enabling the scalable synthesis of titania supported ultrasmall low-valent copper catalysts for efficient photocatalytic activation of peroxymonosulfate, Nanoscale 13 (32) (2021) 13764–13775, https://doi.org/10.1039/D1NR03535E.

[94] H. Cai, M. Chen, J. Li, Y. Jin, Y. Ma, Q. Ma, P. Zhu, Insight into the activation of persulfate with cu2o/visible-light: cu(i) based photo-fenton and cu2o surface mediated free radical mechanism, Mater. Sci. Semicond. Process. 143 (2022) 106502, https://doi.org/10.1016/j.mssp.2022.106502.

[95] A.A. Nada, W. Nasr, R. Viter, P. Miele, S. Roualdes, M. Bechelany, A.A. Nada, H.H. El-Maghrabi, B.A. Koiki, M. Rivallin, M.F. Bekheet, R. Viter, D. Damberga, G. Lesage, I. Iatsunskyi, E. Coy, M. Cretin, O.A. Arotiba, M. Bechelany, Photoelectrocatalysis of paracetamol on Pd–ZnO/ N-Doped carbon nanofibers electrode, Appl. Mater. Today 24 (2021) 101129, https://doi.org/10.1016/j.apmt.2021.101129.

[96] S.O. Ganiyu, N. Oturan, S. Raffy, M. Cretin, C. Causserand, M.A. Oturan, Efficiency of Plasma elaborated sub-stoichiometric titanium oxide (ti4o7) ceramic electrode for advanced electrochemical degradation of paracetamol in different electrolyte media, Sep. Purif. Technol. 208 (2019) 142–152, https://doi.org/10.1016/j.seppur.2018.03.076.

[97] L.C. Almeida, S. Garcia-Segura, N. Bocchi, E. Brillas, Solar photoelectro-fenton degradation of paracetamol using a flow plant with a pt/air-diffusion cell coupled with a compound parabolic collector: process optimization by response surface methodology, Appl. Catal. B Environ. 103 (1–2) (2011) 21–30, https://doi.org/10.1016/j.apcatb.2011.01.003.

[98] H. Olvera-Vargas, J.-C. Rouch, C. Coetsier, M. Cretin, C. Causserand, Dynamic cross-flow electro-fenton process coupled to anodic oxidation for wastewater treatment: application to the degradation of acetaminophen, Sep. Purif. Technol. 203 (2018) 143–151, https://doi.org/10.1016/j.seppur.2018.03.063.

[99] M.D.G. de Luna, M.L. Veciana, C.-C. Su, M.-C. Lu, Acetaminophen degradation by electro-fenton and photoelectro-fenton using a double cathode electrochemical cell, J. Hazard. Mater. 217–218 (2012) 200–207, https://doi.org/10.1016/j.jhazmat.2012.03.018.

[100] Q. Sun, Y.-P. Peng, H. Chen, K.-L. Chang, Y.-N. Qiu, S.-W. Lai, Photoelectrochemical oxidation of ibuprofen via Cu2O-Doped TiO2 nanotube arrays, J. Hazard. Mater. 319 (2016) 121–129, https://doi.org/10.1016/j.jhazmat.2016.02.078.

[101] J.-L. Chen, M.-M. Liu, S.-Y. Xie, L.-J. Yue, F.-L. Gong, K.-M. Chai, Y.-H. Zhang, Cu2O-Loaded TiO2 heterojunction composites for enhanced photocatalytic h2 production, J. Mol. Struct. 1247 (2022) 131294, https://doi.org/10.1016/j.molstruc.2021.131294.

[102] J. Zhang, D. Wang, S. Shi, W. Hao, C. Yuan, Z. Lu, F. Teng, Synthesis and photocatalytic activity of cu2o hollow nanospheres/tio2 nanosheets by an in-situ water-bath method, J. Alloys Compd. 899 (2022) 163252, https://doi.org/10.1016/j.jallcom.2021.163252.

[103] T. Yan, T. Wu, Y. Zhang, M. Sun, X. Wang, Q. Wei, B. Du, Fabrication of In2S3/Zn2GeO4 composite photocatalyst for degradation of acetaminophen under visible light, J. Colloid Interface Sci. 506 (2017) 197–206, https://doi.org/10.1016/j.jcis.2017.06.079.

[104] L. Wang, Z. Bian, Photocatalytic degradation of paracetamol on pd–bivo4 under visible light irradiation, Chemosphere 239 (2020) 124815, https://doi.org/10.1016/j.chemosphere.2019.124815.

[105] X. Xiao, R. Hu, C. Liu, C. Xing, C. Qian, X. Zuo, J. Nan, L. Wang, Facile large-scale synthesis of β-bi2o3 nanospheres as a highly efficient photocatalyst for the degradation of acetaminophen under visible light irradiation, Appl. Catal. B Environ. 140–141 (2013) 433–443, https://doi.org/10.1016/j.apcatb.2013.04.037.

[106] K. Li, J. Chen, Y. Ao, P. Wang, Preparation of a Ternary G-C3N4-CdS/Bi4O5I2 composite photocatalysts with two charge transfer pathways for efficient degradation of acetaminophen under visible light irradiation, Sep. Purif. Technol. 259 (2021) 118177, https://doi.org/10.1016/j.seppur.2020.118177.

[107] K. Chen, X. Wang, P. Xia, J. Xie, J. Wang, X. Li, L. Li, Efficient removal of 2, 2′, 4, 4′-tetrabromodiphenyl ether with a Z-scheme Cu2O-(rGO-TiO2) photocatalyst under sunlight irradiation, Chemosphere 254 (2020) 126806.

[108] Y. Li, K. Chen, X. Wang, Z. Xiao, G. Liao, J. Wang, L. Li, Efficient removal of TBBPA with a Z-scheme BiVO4-(rGO-Cu2O) photocatalyst under sunlight irradiation, Chemosphere 308 (2022) 136259.

[109] M. Yu, M. Tang, Y. Liao, W. He, X.X. Lu, X. Li, Defect-designed Mo-doped BiVO4 photoanode for efficient photoelectrochemical degradation of phenol, J. Mater. Sci. Technol. (2023).